

Accepted for publication in the Astronomical Journal

ALFALFA Discovery of the Nearby Gas-rich Dwarf Galaxy Leo P. V. Neutral Gas Dynamics and Kinematics

Elijah Z. Bernstein-Cooper

Department of Astronomy, University of Wisconsin, 475 N Charter St Madison, WI 53706, USA; Department of Physics & Astronomy, Macalester College, 1600 Grand Avenue, Saint Paul, MN 55105, USA

`ezbc@astro.wisc.edu`

John M. Cannon

Department of Physics & Astronomy, Macalester College, 1600 Grand Avenue, Saint Paul, MN 55105, USA

`jcannon@macalester.edu`

Edward C. Elson

Astrophysics, Cosmology and Gravity Centre (ACGC), Department of Astronomy, University of Cape Town, Private Bag X3, Rondebosch 7701, South Africa

`elson.e.c@gmail.com`

Steven R. Warren

Department of Astronomy, University of Maryland, CSS Bldg., Rm. 1024, Stadium Dr., College Park, MD 20742-2421, USA

`swarren@astro.umd.edu`

Jayaram Chengalur

National Centre for Radio Astrophysics, TIFR, Post Bag 3, Ganeshkhind, Pune 411 007, India

`chengalur@ncra.tifr.res.in`

Evan D. Skillman

*Minnesota Institute for Astrophysics, School of Physics and Astronomy, University of
Minnesota, 116 Church St. SE, Minneapolis, MN 55455, USA*

`skillman@astro.umn.edu`

Elizabeth A. K. Adams

*Center for Radiophysics and Space Research, Space Sciences Building, Cornell University,
Ithaca, NY 14853, USA*

*Netherlands Institute for Radio Astronomy (ASTRON), Postbus 2, 7990 AA, Dwingeloo,
The Netherlands*

`betsey@astro.cornell.edu`

Alberto D. Bolatto

*Department of Astronomy, University of Maryland, CSS Bldg., Rm. 1024, Stadium Dr.,
College Park, MD 20742-2421, USA*

`bolatto@astro.umd.edu`

Riccardo Giovanelli

*Center for Radiophysics and Space Research, Space Sciences Building, Cornell University,
Ithaca, NY 14853, USA*

`riccardo@astro.cornell.edu`

Martha P. Haynes

*Center for Radiophysics and Space Research, Space Sciences Building, Cornell University,
Ithaca, NY 14853, USA*

`haynes@astro.cornell.edu`

Kristen B. W. McQuinn

*Minnesota Institute for Astrophysics, School of Physics and Astronomy, University of
Minnesota, 116 Church St. SE, Minneapolis, MN 55455, USA*

`kmcquinn@astro.umn.edu`

Stephen A. Pardy

Department of Astronomy, University of Wisconsin, 475 N Charter St Madison, WI 53706, USA; Department of Physics & Astronomy, Macalester College, 1600 Grand Avenue, Saint Paul, MN 55105, USA

`spardy@astro.wisc.edu`

Katherine L. Rhode

Department of Astronomy, Indiana University, 727 East Third Street, Bloomington, IN 47405, USA

`rhode@astro.indiana.edu,`

John J. Salzer

Department of Astronomy, Indiana University, 727 East Third Street, Bloomington, IN 47405, USA

`slaz@astro.indiana.edu`

ABSTRACT

We present new HI spectral line imaging of the extremely metal-poor, star-forming dwarf irregular galaxy Leo P. Our HI images probe the global neutral gas properties and the local conditions of the interstellar medium (ISM). The HI morphology is slightly elongated along the optical major-axis. We do not find obvious signatures of interaction or infalling gas at large spatial scales. The neutral gas disk shows obvious rotation, although the velocity dispersion is comparable to the rotation velocity. The rotation amplitude is estimated to be $V_c = 15 \pm 5$ km s^{-1} . Within the HI radius probed by these observations, the mass ratio of gas to stars is roughly 2:1, while the ratio of the total mass to the baryonic mass is $\gtrsim 15:1$. We use this information to place Leo P on the baryonic Tully-Fisher relation, testing the baryonic content of cosmic structures in a sparsely populated portion of parameter space that has hitherto been occupied primarily by dwarf spheroidal galaxies. We detect the signature of two temperature components in the neutral ISM of Leo P; the cold and warm components have characteristic velocity widths of 4.2 ± 0.9 km s^{-1} and 10.1 ± 1.2 km s^{-1} , corresponding to kinetic temperatures of ~ 1100 K and ~ 6200 K, respectively. The cold HI component is unresolved at a physical resolution of 200 pc. The highest HI surface densities

are observed in close physical proximity to the single H II region. A comparison of the neutral gas properties of Leo P with other extremely metal-deficient (XMD) galaxies reveals that Leo P has the lowest neutral gas mass of any known XMD, and that the dynamical mass of Leo P is more than two orders of magnitude smaller than any known XMD with comparable metallicity.

Subject headings: galaxies: evolution — galaxies: dwarf — galaxies: irregular — galaxies: individual (Leo P)

1. Introduction

The exploration of the neutral interstellar medium (ISM) of star-forming, low-mass galaxies has become a major observational and theoretical focus of extragalactic astrophysics. Motivated by the long-standing “missing satellites” problem (Kauffmann et al. 1993; Klypin et al. 1999; Moore et al. 1999) and by recent extensions of the baryonic Tully-Fisher relationship to low rotation velocities (e.g., Stark et al. 2009; McGaugh et al. 2010; McGaugh 2012), major interferometric survey programs have been undertaken to characterize the morphology and dynamics of individual gas-rich dwarfs in the Local Volume (THINGS, Walter et al. 2008; FIGGS, Begum et al. 2008b; SHIELD, Cannon et al. 2011; VLA-ANGST, Ott et al. 2012; LITTLE THINGS, Hunter et al. 2012). Based on the results of these surveys, star-forming galaxy disks with neutral hydrogen masses exceeding $\sim 10^7 M_{\odot}$ are numerous, well-studied, and comparatively well-understood.

In contrast, the parameter space of the most extremely low-mass and gas-rich systems remains only sparsely investigated. The review of McConnachie (2012) lists 12 systems in or near the Local Group with detected neutral hydrogen masses $M_{\text{HI}} < 10^6 M_{\odot}$ (dSph or dE/dSph systems including Sculptor, Fornax, NGC 205, and NGC 185; “transition” objects classified as dIrr/dSph including LGS 3, Phoenix, Leo T, UGC 4789, ESO 410-G 005, and ESO 294-G 010; and dIrr systems including Antlia and KKH 86). Together, the aforementioned major surveys add a few more systems with $M_{\text{HI}} < 10^6 M_{\odot}$ (LGS 3 was observed in the LITTLE THINGS survey, and Antlia, KDG 73, KKH 86, and KK 230 were observed in the VLA-ANGST project). Similarly, selected individual systems outside of the Local Group have also been discovered recently: Roychowdhury et al. (2012) catalog dJ0926+7030 and dJ1012+64 (which appears to be UGC 5497 via cross-listing in the NASA Extragalactic Database) as blue compact dwarf systems in the M 81 group. To our knowledge, this is the complete sample of presently known galaxies with detected neutral hydrogen masses $< 10^6 M_{\odot}$ (excluding Leo P, the subject of this paper). To date, none of these systems has been the subject of a detailed mass distribution analysis.

One of the primary goals of the Arecibo Legacy Fast ALFA (ALFALFA) blind extragalactic HI survey is to populate the faint end of the HI mass function with statistical confidence (Giovanelli et al. 2005). Major follow-up survey programs targeting ALFALFA detections are underway, sampling low-mass, HI-rich systems that both possess and lack obvious stellar counterparts in moderate-depth optical survey data products: SHIELD (Cannon et al. 2011) and the “ultra-compact high velocity cloud” (“UCHVC”) sample (Adams et al. 2013). Given the extremely faint optical luminosities of most of the objects in this mass range, the latter initiative may be an especially promising avenue by which to discover new low-mass galaxies in the Local Volume. The challenge is that accurate distances must also be established through detection of their associated stellar populations. As discussed in Adams et al. (2013), if optical imaging reveals a stellar component and a distance within ~ 1 Mpc, then dozens of the candidate UCHVCs could in fact be nearby dwarf galaxies.

Recently, the ALFALFA survey discovered the galaxy known as Leo P from its HI signature alone (Giovanelli et al. 2013). The HI structural parameters of Leo P are consistent with it being classified as a UCHVC according to the criteria in Adams et al. (2013). Subsequent optical imaging (Rhode et al. 2013) and spectroscopy (Skillman et al. 2013) have shown that this system is among the most extreme star-forming systems known in the local universe (see Table 1 for a summary of physical parameters). Located at a distance of $1.72_{-0.40}^{+0.14}$ Mpc (i.e., outside but in the immediate vicinity of the Local Group; McQuinn et al. 2013), this system harbors both young and old stellar populations, as well as a single HII region whose nebular oxygen abundance (measured by the direct line method in Skillman et al. 2013) is only 3% Z_{\odot} ; this is equal within the uncertainties to that of IZw 18 (Skillman & Kennicutt 1993) and DDO 68 (Berg et al. 2012). The combination of the very small total luminous baryonic mass ($M_{\text{HI}} = 9.1 \times 10^5 M_{\odot}$; $M_{\star} = 5.7 \times 10^5 M_{\odot}$), the presence of ongoing star formation, the extremely low oxygen abundance, and the relative isolation (the nearest known neighbor, Sextans B, is $0.47_{-0.24}^{+0.14}$ Mpc away in 3D space; see details in McQuinn et al. 2013), make Leo P unique among nearby dwarf galaxies. It represents an ideal opportunity to understand numerous facets of galaxy evolution, including the nature of star formation in the metal-poor ISM, the phase structure of the ISM, the dynamics of extremely low-mass gaseous disks, and the baryonic content of low-mass halos.

In this fifth paper in the series of manuscripts about Leo P (papers one through four are Giovanelli et al. 2013, Rhode et al. 2013, Skillman et al. 2103, and McQuinn et al. 2013, respectively; paper six by Warren et al., in preparation, presents CARMA CO imaging of Leo P), we study the neutral gas morphology and dynamics of Leo P. We organize this manuscript as follows. In § 2 we describe the data acquisition, reduction and analysis. § 3 presents the HI morphology and kinematics, while § 4 discusses the rotation of Leo P. In § 5 we derive the properties of the cold and warm ISM in Leo P. § 6 places Leo P in context

amongst other metal-poor galaxies. In § 7 we present our conclusions.

2. Observations and Data Handling

We acquired three sets of HI 21-cm spectral-line observations with the *Karl G. Jansky Very Large Array*¹ (VLA). C-configuration (VLA/C) and B-configuration (VLA/B) observations were acquired in April and August of 2012, respectively, for Director’s Discretionary Time program VLA/12A-456 (AC1105; PI Cannon). D-configuration (VLA/D) observations were acquired in March of 2013 for program VLA/13A-026 (AC1114; PI Cannon). We centered an IF-band on 1419.04 MHz and used a bandwidth of 1,000 kHz (4,000 kHz for VLA/D) with 256 channels (1,000 for VLA/D), resulting in a spectral channel separation of 3.9 kHz ($0.83 \text{ km s}^{-1} \text{ ch}^{-1}$). The primary calibrator was 3C286 and the phase calibrator was J12021+2159. Total on-source integration times amounted to 5 hours in the B-configuration, and 3 hours each in the C- and D-configurations. Unfortunately, the B-configuration observations were compromised by a class M5.5 solar flare that occurred on August 18, 2012²; Leo P was less than 9° from the Sun during these observations.

Giant Metrewave Radio Telescope (GMRT) observations of Leo P were conducted in December of 2012, amounting to 20.5 hours of on-source integration time. We implemented a similar observational set-up to the VLA observations, the primary difference being that the GMRT observations had a spectral resolution of 8.13 kHz ($1.72 \text{ km s}^{-1} \text{ ch}^{-1}$).

We calibrated each dataset individually via standard prescriptions using CASA³ and AIPS⁴ for the VLA observations. The initial calibration and flagging of the GMRT data was done using the flagcal package (Prasad & Chengalur 2012; Chengalur 2013). We subtracted the continuum from each uv -dataset using a first-order linear fit leaving only the line source. We smoothed all datasets to a common spectral channel separation of $2.5 \text{ km s}^{-1} \text{ ch}^{-1}$ by using CASA to shift all input databases to the same spectral grid in the Local Standard of Rest frame. We then concatenated all of the data into a single uv database; all uv weights were set to unity during concatenation.

Next, we inverted and imaged all four uv -datasets together in the AIPS environment. We

¹The National Radio Astronomy Observatory is a facility of the National Science Foundation operated under cooperative agreement by Associated Universities, Inc.

²<http://www.swpc.noaa.gov>

³Common Astronomy Software Application (CASA) is developed and maintained by the NRAO.

⁴Astronomical Image Processing System (AIPS) is developed and maintained by the NRAO.

used a Gaussian weighting scheme of shorter and longer baselines in the uv -plane to produce four cubes with beam areas increasing by a factor of four. We also produced a cube with $24''$ (200 pc) resolution to facilitate direct comparison with previous work (see detailed discussion in § 5). We performed residual flux rescaling on each of the cubes in order to account for the different shapes of the clean beam and the dirty beam (Jorsater & van Moorsel 1995). These cubes were spatially convolved with elliptical Gaussian functions to produce circular beam sizes of $4''$, $8''$, $16''$, $24''$, and $32''$; these cubes have root-mean-square (RMS) noises (measured in line-free channels of the non-rescaled cubes) of 0.45, 0.40, 0.51, 0.64, and 0.66 mJy beam $^{-1}$, respectively.

We derived moment maps and the global profile for each of the cubes by following the THINGS protocols described in Walter et al. (2008). We began by spatially convolving the cube to twice the resolution and then blanking at the 2.5σ level in the new cube. Next, we hand-blanked this cube and used it as a mask to blank the original cube. We integrated all emission in the masked original resolution cube to create the moment zero map. Moment one and moment two maps were derived by including all emission in the masked original resolution cube above the 5σ level. The integrated HI spectrum was derived from the masked original resolution cube. All velocity information presented is calculated in the Local Standard of Rest frame. HI column density maps were calculated assuming optically thin HI gas.⁵ Note that second moment maps made from datacubes blanked in this way provide lower limits to the velocity dispersions, particularly in regions of low signal-to-noise.

3. Gaseous, Stellar, and Dark Components

3.1. Neutral Gas Morphology

In Figure 1 we present individual channel maps of the HI emission at $16''$ resolution. HI emission is detected across roughly 40 km s^{-1} of velocity space ($\sim 240 \text{ km s}^{-1}$ - 280 km s^{-1}). The full (non-blanked) cube is shown in order to convey the relative signal to noise ratio in each channel of the cube. There is a signature of rotation in these panels, evidenced by the position of the HI maximum in each panel moving slightly from northwest to southeast at progressively higher recessional velocities.

We create global HI profiles for Leo P by summing the flux in each of the blanked datacubes and plotting versus velocity in Figure 2. The left panel compares the $32''$ resolution

⁵For optically thin HI gas, $N_{\text{HI}} = 1.823 \times 10^{18} \int T_b d\nu \text{ cm}^{-2}$ where T_b is brightness temperature and ν is frequency.

profile with those derived from the ALFALFA data products as well from the follow-up confirmation observation with the L-band Wide receiver at Arecibo (from which an HI global flux integral of $1.31 \pm 0.04 \text{ Jy km s}^{-1}$ is derived; see Giovanelli et al. 2013 for details). There is good agreement of these profiles, both in terms of the line profile shapes and in terms of the recovered flux integrals. The right panel shows the global profiles at each angular resolution. The global flux densities are 1.03, 0.93, 0.65 and $0.31 \text{ Jy km s}^{-1}$ from the $32''$, $16''$, $8''$, and $4''$ cubes, respectively. As expected, due to masking, the profiles become narrower and recover less flux at successively higher angular resolutions.

The systemic velocity (V_{sys}) of Leo P is estimated using the methods of Springob et al. (2005), as applied in Pardy et al. (2014). We identify the peak flux, f_p , and then fit a first-order polynomial to the rising side of the spectrum using all fluxes between 15% and 85% of f_p . We define V_r as the velocity where the fitted polynomial equals 50% of f_p . We repeat the fit for the falling side of the spectrum, and define V_l in the same way as V_r . The velocity width, W_{50} , is defined as the difference between the velocities V_l and V_r . The systemic velocity, V_{sys} , is then the average of V_l and V_r weighted by the flux. Leo P has a systemic velocity of $V_{\text{sys}} = 260.8 \pm 2.5 \text{ km s}^{-1}$ in the Local Standard of Rest Kinematic (LSRK) frame and a full-width half-maximum of $W_{50} = 22.5 \pm 3.7 \text{ km s}^{-1}$.

HI moment zero images, representing HI column density or HI mass surface density, are presented in Figures 3, 4, and 5. In Figure 3, the HI moment zero images at each angular resolution are shown in greyscale, with contours overlaid. These same contours are then overlaid on the optical broad-band image from the Large Binocular Telescope (LBT⁶) in Figure 4; this optical image was originally presented in McQuinn et al. (2013). Similarly, in Figure 5, the HI moment zero image at $4''$ resolution is compared with the same LBT image as in Figure 4, as well as with the H α image from the KPNO 2.1m telescope from Rhode et al. (2013).

At low resolution, the peaks in the HI column density correspond to peaks in the stellar surface brightness. Interestingly, as one moves outward from the optical and HI center of the system, there are stars that are associated with Leo P (see the individual star lists in both Rhode et al. 2013 and in McQuinn et al. 2013) that are beyond the regions in which we detect HI gas (most noticeably in the northwest region of the galaxy). Most of these

⁶The LBT is an international collaboration among institutions in the United States, Italy, and Germany. LBT Corporation partners are: The University of Arizona on behalf of the Arizona university system; Istituto Nazionale di Astrofisica, Italy; LBT Beteiligungsgesellschaft, Germany, representing the Max-Planck Society, the Astrophysical Institute Potsdam, and Heidelberg University; The Ohio State University, and The Research Corporation, on behalf of The University of Minnesota, The University of Notre Dame, and The University of Virginia.

outlying stars to the northwest are older red giant stars; the blue main-sequence stars in Leo P are concentrated in the region occupied by the high surface density gas in Figure 4. There is also a low surface brightness extension of the H I gas to the southeast, inside of which few stars associated with Leo P are detected. We do not interpret these as signatures of tidal interaction, since we see no concrete evidence of H I gas on larger spatial scales when the uv data are imaged with a Gaussian taper to produce spatial resolutions larger than $32''$ (further, recall the discussion of the relative isolation of Leo P in § 1). A deep single-dish H I mapping mosaic of the region surrounding Leo P would provide more stringent constraints on the nature of any tidal interaction Leo P may have undergone; ALFALFA mapping has not revealed any gas-bearing feature in the vicinity of Leo P.

A considerable amount of the H I gas in Leo P lies in central regions of high surface-brightness H I. Moving to progressively higher spatial resolutions, the H I becomes increasingly localized around the highest surface brightness stellar components of the galaxy. As Figure 5 shows, the highest H I column densities ($N_{\text{HI}} \gtrsim 4 \times 10^{20} \text{ cm}^{-2}$, corresponding to an H I mass surface density $\sigma_{\text{HI}} > 3.2 \text{ M}_{\odot} \text{ pc}^{-2}$) are mostly co-spatial with the youngest massive stars identified in Rhode et al. (2013) and in McQuinn et al. (2013). Two regions reach a peak H I column density of 6.5×10^{20} ($5.2 \text{ M}_{\odot} \text{ pc}^{-2}$); one is nearly cospatial with the single H II region, while a second peak is located slightly offset from the main stellar component. This latter peak is not currently associated with ongoing star formation.

Molter et al. (2014) and Warren et al. (2014) report sensitive new *Combined Array for Research in Millimeter-wave Astronomy* (CARMA) CO (1-0) observations of Leo P. A detailed comparison of those CO upper limits with the present H I and optical data will allow unique tests of models of star formation in the extremely metal-poor ISM. We defer such analyses to Warren et al. (2014).

3.2. Neutral Gas Kinematics

The $16''$ resolution H I moment zero images are compared with the moment one (intensity-weighted velocity field) and with the moment two (H I velocity dispersion) images in panels (a), (c), and (e) of Figure 6. The moment one map reveals an obvious but low-amplitude ($\lesssim 15 \text{ km s}^{-1}$) velocity gradient from the northwest to the southeast regions of Leo P. However, the moment one map is relatively noisy and does not show a simple velocity field; significant random motions are superposed on the bulk rotation signature. This is unlike the regular rotation seen in some more massive dIrr galaxies (e.g., Ott et al. 2012; Hunter et al. 2012).

Part of the disorder of the velocity field shown in Figure 6 can be accounted for by Leo P’s velocity dispersion. The moment two map (also shown in Figure 6) indicates that the velocity dispersion is $\gtrsim 8 \text{ km s}^{-1}$ throughout the disk of Leo P. Superposed on this narrow dispersion gas is a component with velocity dispersions of $10\text{--}12 \text{ km s}^{-1}$. These velocity dispersion values are comparable to those seen in other dwarf galaxies (see, e.g., the discussion in Warren et al. 2012 and Stilp et al. 2013, and references therein). Leo P is similar to some of the lowest-mass gas-rich galaxies studied in Begum et al. (2003), Begum & Chengalur (2004), Begum et al. (2008), Ott et al. (2012), and references therein, where the average velocity dispersion across the disk is comparable to the estimates of the magnitude of the coherent rotational velocity (see § 4).

In order to get a robust estimate of the global velocity dispersion, we fitted Gaussian functions to individual profiles in the datacube. We first spatially binned the $16''$ resolution cube to $6''$ pixels and then fit spectral profiles including emission above 5σ with both one Gaussian and two Gaussians. Double Gaussian fits converged to only a handful of pixels; these results are discussed in § 5 as evidence for two thermally stable phases of the atomic gas. We thus estimate the global velocity dispersion using only single Gaussian fits; the average of the resulting Gaussian fits is 8.4 km s^{-1} , and the standard deviation of the Gaussian widths is 1.4 km s^{-1} . We thus conclude that the global velocity dispersion of Leo P is $8.4 \pm 1.4 \text{ km s}^{-1}$.

A first-order characterization of the rotation of Leo P is available by extracting spatially-resolved position-velocity (PV) slices through the $16''$ resolution datacube. This strategy is similar to the one presented in Cannon et al. (2011b). The kinematic major-axis is identified as that axis along which a PV slice gives the largest projected velocity gradient. This angle, measured counterclockwise from north to the approaching side of the disk, is 335° ; this angle is obvious from the velocity fields presented in Figure 6 and is in agreement with the apparent optical major-axis (see Figures 4 and 5, and the images presented in Rhode et al. 2013 and McQuinn et al. 2013). We extract PV slices through the datacubes, summing all emission in beam-wide areas, each separated by a full beam width. Slices are extracted along both the kinematic major-axis and the kinematic minor-axis. This produces multiple PV slices through the datacube, each of which is independent from its neighbor. The central slice along each axis is centered on the H I column density maximum. The orientations of these slices are shown by arrows overlaid on the moment zero, one, and two images at $16''$ resolution in Figure 6 (b), (d), and (f), respectively.

The spatially-resolved PV slices are shown in Figure 7 for the $16''$ cube. The number of each panel corresponds to the number of the slice in Figure 6; the major-axis slices are shown in the upper panel, and the minor-axis slices are shown in the lower panel. The direction of

the slices is such that a positive angular offset (in Figure 7) corresponds to movement in the direction of the arrows shown in Figure 6.

From these PV slices we draw the following conclusions. First, the velocity extent of the galaxy is comparable along the major-axis and the minor-axis, and is only slightly larger than the central velocity dispersion of the gas (i.e., the projected rotation velocity is of order the velocity dispersion). Second, the minor-axis cuts allow a coarse estimate of velocity and position at different ends of the disk; if this is interpreted as rotation, it sets a lower bound for the rotation velocity (since the PV slices apply no inclination correction). The observed difference in these velocities is $\lesssim 20 \text{ km s}^{-1}$. Taking half of this as the projected rotation, we estimate the rotation amplitude to be $\sim 10 \text{ km s}^{-1}$ or less; we discuss this amplitude further in § 4. Third, there is evidence for localized concentrations of HI with modest velocity widths on the order of the velocity dispersion. These are apparent in both the major-axis and the minor-axis slices, most obviously in the central cuts through the HI column density maxima. Fourth, the extension of HI to the southeast appears as an asymmetry in the PV slices (compare cuts #1 and #5 on the minor-axis; this is also evident in major-axis cut #2).

4. The Rotation of Leo P

Rotation curve work using HI spectral line observations requires both high spectral and high spatial resolution data (i.e., many beams across the disk, with velocity resolution much finer than the magnitude of the velocity gradient across neighboring beams), as well as a galactic disk that has a favorable geometric orientation. Knowing various parameters such as kinematic major-axis angle, systemic velocity, dynamical center position, and inclination, one can fit a series of tilted rings to the observed velocity field that is representative of a thin rotating galactic disk. Such well-constrained rotation curves allow for a detailed analysis of the baryonic-to-dark matter ratio as a function of radius, in addition to constraining the total dynamical mass within the outermost ring.

We were unable to fit a single unambiguous rotation curve to the velocity field of Leo P at any angular resolution without enforcing priors. While the kinematic major-axis angle, systemic velocity, and velocity dispersion are well-constrained by the data, a range of values for the dynamical center, inclination, and rotation velocity were able to return adequate fits to the data. In order to extract dynamical information about Leo P from these data, we thus adopt the value of inclination, $i = 60^\circ$, from Giovanelli et al. (2013). This inclination is based on both the HI and the optical axial ratios. Below we use this value of inclination to estimate the dynamical mass of Leo P.

We have two methods with which to estimate the rotation velocity of Leo P. The first is to exploit the spatially-resolved PV diagrams shown in Figure 7. As discussed in § 3.2, the minor-axis PV slices allow one to measure the projected velocity at either end of the disk. Assuming that the difference in these velocities is caused by the rotation of the system, this provides an estimate of the rotation amplitude, $V_{\text{rot}} \lesssim 10 \text{ km s}^{-1}$. Assuming $i = 60^\circ$ (see above), the inclination correction of $\simeq 15\%$ increases the rotation velocity by less than $\sim 2 \text{ km s}^{-1}$.

The second and more robust method with which to estimate the rotation velocity of Leo P is a major-axis PV slice. The positions of the spatially-resolved PV slices (width equal to the beam size) are shown in Figure 6, and the resulting slices are shown in Figure 7. These panels reveal a total velocity extent of $10 \pm 5 \text{ km s}^{-1}$ for gas above the 3σ level, within $\pm 60''$ of the assumed dynamical center. It is important to note that these major-axis PV slices only include pixels summed over a single beam width.

From these major-axis PV slices, we determine a maximum velocity offset of $\pm 10 \text{ km s}^{-1}$ from systemic, over an angular separation of $\pm 60''$. Specifically, the maximum projected velocity of $\sim 270 \text{ km s}^{-1}$ occurs in the extreme southeast region of the disk, while the minimum projected velocity of $\sim 250 \text{ km s}^{-1}$ occurs in the northwest region of the disk. Along the direction of the PV slice, the maximum offset between these locations is roughly $-1'$ to $+1'$ (corresponding to $\pm 500 \text{ pc}$). This is slightly smaller than the linear extent over which HI is detected; a line with position angle = 335° , passing through the HI column density maximum of the $16''$ moment zero map (see Figure 6) and traversing the entire detected HI extent, has a length of $184''$.

Having constrained the total rotation velocity, we now consider effects that may bear on the interpretation of these results. The first of these is the possible contribution of pressure support to the disk. Given the comparable magnitudes of the projected rotation ($V_{\text{rot}} \sim 10 \text{ km s}^{-1}$; see above) and the velocity dispersion ($8.4 \pm 1.4 \text{ km s}^{-1}$ throughout the disk, with significant regions of the system showing values of $10\text{--}12 \text{ km s}^{-1}$; see Figure 6 and discussion in § 3.2), it is likely that random motions in the neutral gas provide some level of dynamical support within the disk of Leo P.

Traditionally, the effects of pressure support within a galactic disk are modeled by the asymmetric drift correction. One parameterization of this correction (Frusciante et al. 2012) is given by

$$V_c^2(r) = V_{\text{rot}}^2(r) - \sigma^2(r) \left(\frac{d \log \mu(r)}{d \log r} + \frac{d \log \sigma^2(r)}{d \log r} \right) \quad (1)$$

where V_c is the true rotation velocity or circular velocity (corresponding to the true dynamical mass in the absence of pressure support) in km s^{-1} , V_{rot} is the observed gas rotation velocity in km s^{-1} , σ is the velocity dispersion of the gas in km s^{-1} , μ is the gas mass surface density in $M_{\odot} \text{pc}^{-2}$, and r is the radius in pc. The values of μ and σ are usually measured by averaging emission in the moment zero and moment two maps (using the tilted ring parameters derived from rotation curve analysis), fitting the resulting data points with a differentiable function, and evaluating at a given radius. Since we do not have an unambiguous rotation curve for Leo P, we simply used the GIPSY task ELLINT to create radially-averaged profiles of the HI surface brightness and of the HI velocity dispersion. The magnitude of the resulting asymmetric drift correction reaches $\sim 5 \text{ km s}^{-1}$ at a radius of $64''$ (530 pc). As expected based on the comparable magnitudes of the projected rotation velocity and the velocity dispersion, the dynamical support provided by random motions is appreciable.

The second possible effect is beam smearing. The observed rotation amplitude can underestimate the true amplitude if the beam size smoothes over a significant gradient in velocity. To test for the possibility of beam smearing in our data, we used the GIPSY task GALMOD to construct model datacubes with maximum rotation amplitudes of 10 km s^{-1} and 15 km s^{-1} ; the inclination was fixed at 60° . We then smoothed these cubes to $16''$ and $32''$ resolutions. In each case, we are able to differentiate between a 10 km s^{-1} rotator and a 15 km s^{-1} rotator that has been severely beam smeared. We thus conclude that the effects of beam smearing are minor in these data.

Based on the above discussion, we conclude that the circular velocity of Leo P is $15 \pm 5 \text{ km s}^{-1}$. While evidence favors a velocity less than 10 km s^{-1} , the inclination of the source and the significant contribution of pressure support to the disk may allow the true rotation amplitude to reach 15 km s^{-1} .

Perhaps the most critical physical parameters that can be derived from the datasets in hand are the total dynamical mass (within the outermost radius within which HI is detected) and the luminous baryonic mass. Using the angular distance of $60''$ ($r = 500 \text{ pc}$ at 1.72 Mpc) discussed above for the maximum measured radial distance within the disk, and conservatively assuming a circular velocity of $V_c = 15 \text{ km s}^{-1}$ at this radius, a simple $\frac{V_c^2 \cdot r}{G}$ calculation gives a total dynamical mass estimate of $M_{\text{dyn}} > 2.6 \times 10^7 M_{\odot}$. This value is quoted as a lower limit because it only includes the mass within the HI radius; it seems likely that the dark matter halo extends well beyond this radius. The luminous baryonic mass is considered to be the sum of the gas mass and the stellar mass. We implicitly assume that the dust and H_2 contents of Leo P are modest compared to these quantities; this is in agreement with measurements of the dust mass of the extremely metal poor galaxy IZw 18 (Cannon et al. 2002; Herrera-Camus et al. 2012; Fisher et al. 2014). We also assume that the

ionized gas mass in Leo P is negligible compared to the mass of neutral hydrogen. The total gaseous mass ($M_{\text{HI}} + 35\%$ for Helium) of Leo P is found to be $1.2 \times 10^6 M_{\odot}$ (applying the Arecibo value of $S_{\text{HI}} = 1.31 \text{ Jy km s}^{-1}$). As noted above, $M_{\star} = 5.7 \times 10^5 M_{\odot}$. This yields a total baryonic mass of $M_{\text{bary}} = (1.8_{-1.2}^{+0.4}) \times 10^6 M_{\odot}$, where the asymmetric error bars reflect those on the distance measurement from McQuinn et al. (2013).

5. The Cold HI in Leo P

In the first paper in our Leo P series, Giovanelli et al. (2013) postulated that a thermally stable multi-phase neutral ISM may be present in Leo P. They suggested that these phases, if present, have temperatures of $T \lesssim 1,000 \text{ K}$ for the cold phase and $T \gtrsim 6,000 \text{ K}$ for the warm phase. A multi-phase ISM has important implications for models of the ISM in dwarf galaxies whereby the relative masses of the two components may help govern the amount of H_2 formation and the available pressure support (e.g., Pelupessy et al. 2006; Faerman et al. 2013).

To test the hypothesis that two thermally stable HI phases are present in Leo P, we adopted the methods presented in Warren et al. (2012) to search for a cold neutral medium. The method seeks to separate the contribution of the two components in the ISM to the overall spectrum at any given location in a galaxy. For full details of the identification process we refer the reader to Warren et al. (2012); briefly, we first produced image cubes with linear resolutions of 130, 200, and 265 pc ($16''$, $24''$, and $32''$; see below for our justification of these scales). Next we extracted the spectrum from each $1.5''$ pixel and fit both a single and double Gaussian function to those spectra with peak-to-rms S/N > 10 . The residuals of each fit were then compared via a single-tailed F-test and a double Gaussian was deemed a significantly better fit to the data if the probability of improvement was at the $>95\%$ confidence level.

Our choice of linear scales in which to search for the cold HI is driven by both data and physical reasons. Warren et al. (2012) showed that in order to reliably separate multiple Gaussian components one needs to have data with S/N > 10 . Our $4''$ and $8''$ cubes have few pixels that fulfill this basic criterion. Also, in order to separate the cold HI component from the warm HI component, there must be a strong enough cold HI signal. Thus, lower resolution actually helps this procedure. However, if one uses too large a convolution, there arises a risk of diluting the cold HI signal if the beam’s linear scale is much larger than the scales in which the cold HI exists by way of including more of the ubiquitous warm HI component in the spectrum.

Where the cold HI component traces molecular gas, comparisons to current star forma-

tion tracers in the literature show that correlations between $\Sigma(\text{H}_2)$ and $\Sigma(\text{SFR})$ break down on scales below ~ 100 pc (e.g., Onodera et al. 2010). If the molecular clouds in Leo P have similar separation distances as those in the Milky Way (~ 200 pc; Koda et al. 2006), then we would expect to include the flux density of multiple clouds on linear scales of at least this size. For all of the above reasons we fit $16''$, $24''$, and $32''$ cubes (130, 200, and 265 pc linear scales, respectively). The $24'' = 200$ pc cube has the added benefit of allowing us to directly compare to the results in Warren et al. (2012), as they worked at this spatial scale.

We detect the signature of cold HI in the same area in Leo P at each of these spatial scales. The $16'' = 130$ pc detections are slightly resolved as the cold HI is found at 3 independent pixels. The $24'' = 200$ pc and $32'' = 265$ pc cold HI detections are unresolved. Figure 8 shows the spectrum at the location of the peak cold HI component detected in the 200 pc linear resolution data. The cold HI component represents 30% of the total HI flux density at this peak location, which is comparable to the typical 20% flux density contribution seen in Warren et al. (2012). The warm HI component has a Gaussian standard deviation of 10.1 ± 1.2 km s $^{-1}$, while the cold HI component has a Gaussian standard deviation of 4.2 ± 0.9 km s $^{-1}$. These values are typical for the warm and cold HI components seen in many different environments across many different galaxy types (e.g., Young & Lo 1996, 1997; Young et al. 2003; Begum et al. 2006; de Blok & Walter 2006; Tamburro et al. 2009; Warren et al. 2012). Assuming a thermalized distribution of particles without turbulence, these widths correspond to kinetic temperatures of 6,160 K and 1,060 K for the warm and the cold components, respectively. These temperatures are similar to what was predicted by Giovanelli et al. (2013).

In Figure 9 we show the location of the cold HI detection at $24''$ resolution in relation to the integrated HI, the stellar component, and the single HII region in Leo P. The exact location of the cold HI within the beam is uncertain due to the unresolved nature of the emission. However, if molecular material does exist in Leo P, then the encircled area shown in Figure 9 is the most likely place to observe it.

A first order estimate of the mass of HI in the cold component is available by converting the (unresolved) flux density of the cold component, 3.74 Jy Bm $^{-1}$ km s $^{-1}$, into a mass via the standard prescription, $M_{\text{HI}} (M_{\odot}) = 2.36 \times 10^5 S_{\text{HI}} D(\text{Mpc})^2$, where S_{HI} is the flux in units of Jy km s $^{-1}$. This yields $M_{\text{HI,cold}} \geq 9000 M_{\odot}$, which is given as a lower limit, as more cold HI gas could reside on fine spatial scales, where our $8''$ and $4''$ resolution images lack the sensitivity to decompose the HI into warm and cold components. The ratio of cold to total HI mass in Leo P is $\gtrsim 1\%$; this is in general agreement with, although slightly lower than, the corresponding mass ratios found for the galaxies studied in Warren et al. (2012).

The detection of a cold neutral ISM component in Leo P has important implications for

our understanding of the phase structure of the ISM in very low-mass halos. Given that the HI properties of Leo P meet the criteria for classification as a UCHVC (Adams et al. 2013; Giovanelli et al. 2013), it represents a critical testbed for models of the structure of these objects. Modeling of Leo P that is similar to that performed for Leo T in Faerman et al. (2013) would be valuable.

6. Leo P In Context

6.1. Leo P on the Baryonic Tully-Fisher Relation

Since its introduction in the seminal Tully & Fisher (1977) manuscript, the Tully-Fisher relation has become a powerful diagnostic of the physical parameters and distances of galaxies. As shown in Begum et al. (2008), Stark et al. (2009), Trachternach et al. (2009), McGaugh et al. (2010), McGaugh (2012), and references therein, the baryonic Tully-Fisher relationship (BTFR, relating the mass of baryons to the rotation velocity) appears to hold over many orders of magnitude, from galaxy cluster scales down to low-mass gas-rich galaxies.

There has been a long standing interest in extending the Tully-Fisher relationship to the lowest possible rotation velocities. While the use of gas-dominated disk galaxies to derive the slope of the BTFR is well-understood, the extension of the relation to rotation velocities $< 20 \text{ km s}^{-1}$ is challenging. As discussed in detail above for Leo P, and in the literature for other extremely low-mass galaxies (e.g., Leo A, Young & Lo 1996), the low rotation velocities of gas-rich, metal-poor systems make rotation curve work difficult. Only a few low-amplitude rotators ($v_{\text{flat}} \leq 20 \text{ km s}^{-1}$; see discussion in Begum et al. 2008a) are included in the McGaugh (2012) analysis: DDO 210 ($v_{\text{flat}} = 17 \pm 4 \text{ km s}^{-1}$), Camelopardalis B ($v_{\text{flat}} = 20 \pm 12 \text{ km s}^{-1}$), and UGC 8215 ($v_{\text{flat}} = 20 \pm 6 \text{ km s}^{-1}$). Some previous versions of the BTFR have included dSph galaxies at the lowest masses; however, McGaugh & Wolf (2010) argue that some dSphs deviate substantially from the BTFR, and suggest that the environment of these galaxies plays a significant role in this departure.

Given these challenges, the addition of even one more low-amplitude rotator to the BTFR represents a significant step forward. To this end, in Giovanelli et al. (2013) we presented a first estimate of the location of Leo P on the BTFR as calibrated by McGaugh (2012). With the present analysis, we are now able to place Leo P on this plot with confidence. In Figure 10 we thus show two reproductions of the BTFR from McGaugh (2012). Figure 10(a) shows Leo P (turquoise square) amongst all of the galaxies from McGaugh (2012); red circles are star-dominated galaxies, green triangles are gas-rich galaxies, and

blue squares are dSph galaxies. Figure 10(b) shows the same data, but with the dSph galaxies removed (see discussion above and in McGaugh & Wolf 2010 and Stringer et al. 2010) and the dynamic range compressed for ease of interpretation. The shaded grey line shows the $\pm 1\sigma$ regression to the properties of the gas-dominated galaxies derived in McGaugh (2012). The position of Leo P on the BTFR plots is now well-established, based on the estimate of the rotational velocity derived in § 4. The baryonic mass includes both atomic gas (corrected for helium) and stars (derived by McQuinn et al. 2013a). We have made no corrections for molecular gas mass (see details in Molter et al. 2014 and Warren et al. 2014) or for ionized gas mass; note that Gnedin (2012) cautions that the ionized gas component is a substantial mass component in dwarf galaxies.

The position of Leo P in the BTFR is now well-understood. Within the adopted errorbars on the circular velocity and the baryonic mass, Leo P lies just within the 1σ region of the regression derived by McGaugh (2012) and shown in Figure 10. Its baryonic mass is the lowest of any galaxy to date with an estimate of its circular velocity derived from HI observations.

6.2. The Association Between Leo P and the 14+12 Group

McQuinn et al. (2013) first identified the likely membership of Leo P in the 14+12 group, which consists of NGC 3109, Antlia, Sextans A, Sextans B, and GR 8 (Tully et al. 2002). These systems span a range of distances between 1.25 – 1.44 Mpc; McQuinn et al. (2013) show that Leo P lies at one end of this loose association. Sextans B is the closest known neighbor to Leo P, located $0.47_{-0.24}^{+0.14}$ Mpc away in 3D space. These findings were subsequently verified by Bellazzini et al. (2013) and are further discussed in Pawlowski & McGaugh (2014).

Given the loose nature of the 14+12 association, and the large distance between Leo P and Sextans B, it seems unlikely that the inclusion of Leo P in this association has had a measurable impact on its recent evolution. In the HI data presented in this work, we do not find evidence for extended neutral hydrogen gas that would be indicative of an interaction. As argued in McQuinn et al. (2013), Leo P remains an ideal example of a metal-poor galaxy that is evolving in isolation.

6.3. Leo P Compared To Other Extremely Metal Deficient Galaxies

Leo P is one of the most extremely metal-deficient galaxies known in the local universe. As discussed in Berg et al. (2012) and Skillman et al. (2013), the number of “extremely metal

deficient” galaxies (“XMDs”, systems with $12 + \log(\text{O}/\text{H}) \leq 7.65$ or $Z \leq 9\% Z_{\odot}$ using the Solar oxygen abundance of $12 + \log(\text{O}/\text{H}) = 8.69 \pm 0.05$ from Asplund et al. 2009) remains small. Here we compare the neutral gas properties of Leo P with those of the other systems studied in the Berg et al. (2012) sample. The galaxies in that investigation have secure distances, and have error weighted average nebular oxygen abundances, derived using the “direct” method via the auroral $[\text{O III}] \lambda 4363 \text{ \AA}$ emission line, that meet the XMD abundance criterion within observational errors. We supplement this sample with characteristics of the well-studied metal-poor galaxies IZw 18 and SBS 0335-052 taken from the literature.

In Table 2 we summarize relevant physical parameters of these systems. Column 1 gives the name(s) of the galaxy; column 2 gives the error weighted average oxygen abundance on the $12 + \log(\text{O}/\text{H})$ scale; column 3 gives the total HI mass of the galaxy; column 4 gives the stellar mass of the galaxy; column 5 lists the literature references used to compile the table. We do not quote error bars on most values because of the heterogeneity of the datasets used to accumulate the data; some HI masses are derived via interferometric measurements while others use single-dish data, etc. The stellar masses of all systems are derived from Spitzer $4.5 \mu\text{m}$ imaging, except for SBS 0335-052, IZw 18, and Leo P. Since the nebular oxygen abundances of SBS 0335-052E and SBS 0335-052W differ, we treat each component as a separate XMD system.

In Figure 11 we plot these parameters as functions of oxygen abundance for the XMD galaxies. Figures 11(a) and (b) show the HI mass and the stellar mass as functions of the oxygen abundance. Leo P has the lowest neutral hydrogen and stellar mass of any of the 22 XMD systems in Table 2. It is important to stress that this is not simply a proximity effect; some of the systems in this sample are in the Local Group. In Figure 11(c) we plot the M_{HI}/M_{\star} ratio as a function of oxygen abundance. A Spearman’s correlation test reveals a $>99\%$ confidence correlation between higher neutral gas fractions and decreasing oxygen abundances, although the scatter is large at all metallicities. It is interesting to note that even though the HI and stellar masses of Leo P are very low, the M_{HI}/M_{\star} ratio is not abnormal compared to the rest of the sample members.

We are also interested in a comparison of the dynamical properties of these systems and how these vary as a function of metallicity. However, such a comparative analysis was not feasible using the data available in the literature. Only a few of the XMD systems in Table 2 have meaningful estimates of the maximum rotation velocity; further, those that do vary considerably in technique (e.g., formal rotation curve analysis or representative rotation via PV slices, differing numbers of beams across the major-axis, etc.). Given this inhomogeneity, we do not include this data in Table 2, and simply summarize these properties for a few systems below.

The most complete set of dynamical parameters is available for the few most metal-poor systems in the sample. Specifically, for the eight systems with $12 + \log(\text{O}/\text{H}) < 7.5$ (again, SBS 0335-052W and SBS 0335-052E are treated as separate systems), dynamical parameters (including a measurement of rotational velocity and an estimate of the dynamical mass within the H I radius) are available for five: SBS 0335-052W ($V_c \simeq 40 \text{ km s}^{-1}$; $M_{\text{dyn}} \simeq 7.9 \times 10^9 M_\odot$; Ekta et al. 2009), Leo P ($V_c \simeq 15 \text{ km s}^{-1}$; $M_{\text{dyn}} > 2.6 \times 10^7 M_\odot$; this work), IZw 18 ($V_c \simeq 44 \text{ km s}^{-1}$; $M_{\text{dyn}} \simeq 8.6 \times 10^9 M_\odot$; van Zee et al. 1998), UGC 5340 ($V_c \simeq 48\text{-}55 \text{ km s}^{-1}$; $M_{\text{dyn}} \simeq 6.0 \times 10^9 M_\odot$; Ekta et al. 2008), SBS 0335-052E ($V_c \simeq 40 \text{ km s}^{-1}$; $M_{\text{dyn}} \simeq 7.0 \times 10^9 M_\odot$; Ekta et al. 2009). It is interesting to note that the dynamical properties of Leo P are extreme even when compared to those in systems with similar oxygen abundances: the dynamical mass of Leo P (within the H I radius) is more than two orders of magnitude smaller than that of any other system.

It is interesting to note that while we do not find evidence for extended neutral hydrogen gas that would be indicative of infall or of an interaction in Leo P, many (but not all) of the systems in Table 2 do show such morphological or kinematic signatures (see references in Table 2). The trend for XMD systems to preferentially harbor disturbed H I disks was interpreted by Ekta & Chengalur (2010) as empirical evidence that infall of pristine gas may result in lower abundances and lower effective yields. A holistic dynamical and morphological analysis of all known XMD galaxies is beyond the scope of this work, but could be a very promising method with which to establish the fundamental characteristics (e.g., baryon fraction, mass to light ratios, role of inall and interactions) of the most metal-poor galaxies.

7. Discussion and Conclusions

We have presented new *Very Large Array* (VLA) and *Giant Metrewave Radio Telescope* (GMRT) H I spectral line observations of the extreme star-forming galaxy Leo P. This system was discovered in the Arecibo Legacy Fast ALFA (ALFALFA) survey data products based on its H I characteristics alone. Its global neutral gas properties match those of dozens of other ultra-compact high-velocity clouds (UCHVCs) discovered to date by the ALFALFA survey; follow-up observations are underway that may reveal more Leo P analogs in the local universe.

Our combined H I datasets allow us to study the neutral hydrogen in Leo P at high spectral resolution and on spatial scales from tens of pc to galaxy-wide. The neutral gas morphology of Leo P is smooth on global scales and the highest H I and stellar surface brightnesses are cospatial. A small amount of H I gas extends to the southeast beyond the extent of the stellar population, while in the northwest some stars appear to be exterior to

the H I of the system at the present surface brightness sensitivity level. On progressively finer spatial scales, the H I gas becomes strongly localized in column density peaks with H I surface density maxima in excess of $5 M_{\odot} \text{ pc}^{-2}$. An H I column density maximum of $6.5 \times 10^{20} \text{ cm}^{-2}$ ($5.2 M_{\odot} \text{ pc}^{-2}$) is nearly cospatial (less than one H I beam width, or $\lesssim 30 \text{ pc}$) with the location of the single H II region.

The H I dynamics of Leo P are complex. While ordered rotation is clearly present from an examination of both the datacubes and of the intensity-weighted velocity fields at all spatial resolutions, there are significant irregularities that make modeling the neutral gas disk challenging. The velocity dispersion of the disk shows a global value of $8.4 \pm 1.4 \text{ km s}^{-1}$, and some regions show dispersions as large as $10\text{-}12 \text{ km s}^{-1}$.

We derive a low amplitude rotation velocity for Leo P: $V_c \sim 15 \pm 5 \text{ km s}^{-1}$ at $60''$ from the assumed dynamical center. The implied dynamical mass is $M_{\text{dyn}} > 2.6 \times 10^7 M_{\odot}$ interior to the H I radius. The luminous baryonic mass, calculated as the sum of the neutral hydrogen mass (corrected for Helium) and the stellar mass, is $M_{\text{bary}} = (1.8_{-1.2}^{+0.4}) \times 10^6 M_{\odot}$.

Using the techniques described in Warren et al. (2012), we have shown that the neutral ISM of Leo P contains both a cold and a warm component. The cold and warm components have characteristic velocity widths of $4.18 \pm 0.86 \text{ km s}^{-1}$ and $10.08 \pm 1.15 \text{ km s}^{-1}$, corresponding to kinetic temperatures of $\sim 1100 \text{ K}$ and $\sim 6200 \text{ K}$, respectively. The cold H I component is unresolved on 200 pc physical scales. While the exact location of the cold H I in Leo P is uncertain due to the unresolved nature of the emission, if molecular material does exist in Leo P, then it may be cospatial with this cold H I gas.

Leo P has the lowest neutral hydrogen mass and the lowest stellar mass of any of the extremely-metal deficient (XMD) galaxies (systems with $12 + \log(\text{O}/\text{H}) \leq 7.65$) studied in Berg et al. (2012). Interestingly, its ratio of neutral hydrogen mass to stellar mass does not stand out amongst the other XMD galaxies in that work. The dynamical mass of Leo P is more than two orders of magnitude smaller than that of any other system with comparable metallicity. We have placed Leo P on the baryonic Tully-Fisher relation as parameterized in McGaugh (2012); it represents the most slowly-rotating gas-rich galaxy studied to date.

The authors thank the referee for the helpful review of this manuscript. Additionally, we thank the director of the Very Large Array for the positive review of the discretionary time request for program 12A-456, and for the approval of subsequent observations of Leo P in program 13A-026. Some of the observations presented in this paper were obtained using the GMRT which is operated by the National Centre for Radio Astrophysics (NCRA) of the Tata Institute of Fundamental Research (TIFR), India. JMC would like to thank the Istituto Nazionale di Astrofisica and the Osservatorio Astronomico di Padova for their hospitality

during a productive sabbatical leave. We thank R. Koopmann, P. Troischt, and the student members of the Undergraduate ALFALFA team for conducting the confirming L-band wide observations of Leo P. This investigation has made use of the NASA/IPAC Extragalactic Database (NED) which is operated by the Jet Propulsion Laboratory, California Institute of Technology, under contract with the National Aeronautics and Space Administration, and NASA’s Astrophysics Data System.

JMC is supported by NSF grant 1211683. The Undergraduate ALFALFA team is supported by NSF grants AST-0724918, AST-0725267, AST-0725380, AST-0902211, and AST0903394. The ALFALFA work at Cornell is supported by NSF grants AST-0607007 and AST-1107390 to R.G. and M.P.H. and by grants from the Brinson Foundation. E.A.K.A. was supported by an NSF predoctoral fellowship during part of this work. K.L.R. is supported by NSF Faculty Early Career Development (CAREER) award AST-0847109.

REFERENCES

- Adams, E. A. K., Giovanelli, R., & Haynes, M. P. 2013, *ApJ*, 768, 77
- Aloisi, A., Clementini, G., Tosi, M., et al. 2007, *ApJ*, 667, L151
- Asplund, M., Grevesse, N., Sauval, A. J., & Scott, P. 2009, *ARA&A*, 47, 481
- Begum, A., Chengalur, J. N., & Hopp, U. 2003, *New A*, 8, 267
- Begum, A., & Chengalur, J. N. 2004, *A&A*, 413, 525
- Begum, A., Chengalur, J. N., Karachentsev, I. D., Kaisin, S. S., & Sharina, M. E. 2006, *MNRAS*, 365, 1220
- Begum, A., Chengalur, J. N., Karachentsev, I. D., & Sharina, M. E. 2008a, *MNRAS*, 386, 138
- Begum, A., Chengalur, J. N., Karachentsev, I. D., Sharina, M. E., & Kaisin, S. S. 2008a, *MNRAS*, 386, 1667
- Bellazzini, M., Oosterloo, T., Fraternali, F., & Beccari, G. 2013, *A&A*, 559, L11
- Berg, D. A., Skillman, E. D., Marble, A. R., et al. 2012, *ApJ*,
- Bigiel, F., Leroy, A., Walter, F., et al. 2008, *AJ*, 136, 2846
- Cannon, J. M., Skillman, E. D., Garnett, D. R., & Dufour, R. J. 2002, *ApJ*, 565, 931
- Cannon, J. M., et al. 2011a, *ApJ*, 739, L22
- Cannon, J. M., Most, H. P., Skillman, E. D., et al. 2011b, *ApJ*, 735, 35
- Chengalur, J., 2013, NCRA Technical Report NCRA/COM/001
- de Blok, W. J. G., & Walter, F. 2006, *AJ*, 131, 363
- Ekta, Chengalur, J. N., & Pustilnik, S. A. 2008, *MNRAS*, 391, 881
- Ekta, B., Pustilnik, S. A., & Chengalur, J. N. 2009, *MNRAS*, 397, 963
- Ekta, B., & Chengalur, J. N. 2010, *MNRAS*, 406, 1238
- Faerman, Y., Sternberg, A., & McKee, C. F. 2013, *ApJ*, 777, 119
- Feldmann, R., Gnedin, N. Y., & Kravtsov, A. V. 2011, *ApJ*, 732, 115

- Fisher, D. B., Bolatto, A. D., Herrera-Camus, R., et al. 2014, *Nature*, 505, 186
- Frusciante, N., Salucci, P., Vernieri, D., Cannon, J. M., & Elson, E. C. 2012, *MNRAS*, 426, 751
- Giovanelli, R., Haynes, M. P., Adams, E. A. K., et al. 2013, *AJ*, 146, 15
- Giovanelli, R., Haynes, M. P., Kent, B. R., et al. 2005, *AJ*, 130, 2598
- Gnedin, N. Y. 2012, *ApJ*, 754, 113
- Haynes, M. P., Giovanelli, R., Martin, A. M., et al. 2011, *AJ*, 142, 170
- Herrera-Camus, R., Fisher, D. B., Bolatto, A. D., et al. 2012, *ApJ*, 752, 112
- Hunter, D. A., Ficut-Vicas, D., Ashley, T., et al. 2012, *AJ*, 144, 134
- Irwin, M. J., Belokurov, V., Evans, N. W., et al. 2007, *ApJ*, 656, L13
- Izotov, Y. I., Lipovetsky, V. A., Chaffee, F. H., et al. 1997, *ApJ*, 476, 698
- Izotov, Y. I., & Thuan, T. X. 1999, *ApJ*, 511, 639
- Izotov, Y. I., Thuan, T. X., & Guseva, N. G. 2005, *ApJ*, 632, 210
- Jorsater, S., & van Moorsel, G. A. 1995, *AJ*, 110, 2037
- Karachentsev, I. D., Karachentseva, V. E., & Huchtmeier, W. K. 2001, *A&A*, 366, 428
- Kauffmann, G., White, S. D. M., & Guiderdoni, B. 1993, *MNRAS*, 264, 201
- Klypin, A., Kravtsov, A. V., Valenzuela, O., & Prada, F. 1999, *ApJ*, 522, 82
- Koda, J., Sawada, T., Hasegawa, T., & Scoville, N. Z. 2006, *ApJ*, 638, 191
- Liu, G., Koda, J., Calzetti, D., Fukuhara, M., & Momose, R. 2011, *ApJ*, 735, 63
- McConnachie, A. W. 2012, *AJ*, 144, 4
- McGaugh, S. S., Schombert, J. M., de Blok, W. J. G., & Zagursky, M. J. 2010, *ApJ*, 708, L14
- McGaugh, S. S., & Wolf, J. 2010, *ApJ*, 722, 248
- McGaugh, S. S. 2012, *AJ*, 143, 40
- McQuinn, K. B., Skillman, E. D., Berg, D., et al. 2013, *AJ*, 146, 145

- Molter, E., Warren, S. R., Bolatto, A. D., et al. 2014, American Astronomical Society Meeting Abstracts, 223, #246.52
- Moore, B., Ghigna, S., Governato, F., et al. 1999, ApJ, 524, L19
- Nicholls, D. C., Dopita, M. A., Jerjen, H., & Meurer, G. R. 2011, AJ, 142, 83
- Onodera, S., Kuno, N., Tosaki, T., et al. 2010, ApJ, 722, L127
- Ott, J., Stilp, A. M., Warren, S. R., et al. 2012, AJ, 144, 123
- Pardy, S. A., Cannon, J. M., Hayes, M., Östlin, G., et al. 2014, ApJ, submitted
- Pawlowski, M. S., & McGaugh, S. S. 2014, MNRAS, in press (ArXiv/1402.4130)
- Pelupessy, F. I., Papadopoulos, P. P., & van der Werf, P. 2006, ApJ, 645, 1024
- Prasad, J., & Chengalur, J. 2012, Experimental Astronomy, 33, 157
- Pustilnik, S. A., Pramskij, A. G., & Kniazev, A. Y. 2004, A&A, 425, 51
- Rhode, K. L., Salzer, J. J., Haurberg, N. C., et al. 2013, AJ, 145, 149
- Roychowdhury, S., Chengalur, J. N., Chiboucas, K., et al. 2012, MNRAS, 426, 665
- Skillman, E. D. & Kennicutt, R. C. 1993, ApJ, 411, 655
- Skillman, E. D., Salzer, J. J., Berg, D. A., et al. 2013, AJ, 146, 3
- Springob, C. M., Haynes, M. P., Giovanelli, R., & Kent, B. R. 2005, ApJS, 160, 149
- Stark, D. V., McGaugh, S. S., & Swaters, R. A. 2009, AJ, 138, 392
- Stilp, A. M., Dalcanton, J. J., Skillman, E., et al. 2013, ApJ, 773, 88
- Stringer, M., Cole, S., & Frenk, C. S. 2010, MNRAS, 404, 1129
- Tamburro, D., Rix, H.-W., Leroy, A. K., et al. 2009, AJ, 137, 4424
- Trachternach, C., de Blok, W. J. G., McGaugh, S. S., van der Hulst, J. M., & Dettmar, R.-J. 2009, A&A, 505, 577
- Tully, R. B., & Fisher, J. R. 1977, A&A, 54, 661
- Tully, R. B., Somerville, R. S., Trentham, N., & Verheijen, M. A. W. 2002, ApJ, 569, 573
- Walter, F., Brinks, E., de Blok, W. J. G., et al. 2008, AJ, 136, 2563

- Warren, S. R., Skillman, E. D., Stilp, A. M., et al. 2012, ApJ, 757, 84
- Warren, S. R., Molter, E. M, Bolatto, A., Cannon, J. M., et al. 2014, AJ, in preparation
- Wong, T., & Blitz, L. 2002, ApJ, 569, 157
- Young, L. M., & Lo, K. Y. 1996, ApJ, 462, 203
- Young, L. M., & Lo, K. Y. 1997, ApJ, 490, 710
- Young, L. M., van Zee, L., Lo, K. Y., Dohm-Palmer, R. C., & Beierle, M. E. 2003, ApJ, 592, 111
- van Zee, L., Westpfahl, D., Haynes, M. P., & Salzer, J. J. 1998, AJ, 115, 1000

Table 1. Basic Characteristics of Leo P

Parameter	Value	Reference
Right ascension (J2000)	10 ^h 21 ^m 45.1 ^s	Rhode et al. (2013)
Declination (J2000)	+18°05′17.2″	Rhode et al. (2013)
Distance (Mpc)	1.72 ^{+0.12} _{-0.40}	McQuinn et al. (2013)
12+log(O/H)	7.17 ± 0.04	Skillman et al. (2013)
M _V (mag)	-9.37 ^{+0.15} _{-0.50}	McQuinn et al. (2013)
L _{Hα} (erg s ⁻¹)	6.06 × 10 ³⁶	Rhode et al. (2013)
Single-dish S _{HI} (Jy km s ⁻¹)	1.31	Giovanelli et al. (2013)
HI mass M _{HI} (M _⊙)	9.5 × 10 ⁵	Giovanelli et al. (2013), this work
Stellar mass M _★ (M _⊙)	5.7 × 10 ⁵	McQuinn et al. (2013)

Table 2. Properties of Leo P and Selected XMD Galaxies

Galaxy Name(s)	$12+\log(\text{O}/\text{H})$	M_{HI} ($10^6 M_{\odot}$)	M_{\star} ($10^6 M_{\odot}$)	References ^a
SBS 0335-052W	7.12 ± 0.03	580	12.0	1, 2
Leo P	7.17 ± 0.04	0.95	0.57	3, 4, 5
IZw 18	7.17 ± 0.04	230	90	6, 7, 8, 9, 10
UGC 5340 (DDO 68)	7.20 ± 0.05	1,000	93.3	11,12
UGCA 292 (CVn I dwA)	7.30 ± 0.03	40	4.79	11,13
Leo A (DDO 69)	7.30 ± 0.05	6.9	3.80	11, 14
SBS 0335-052E	7.33 ± 0.01	420	41.0	15,2, 16
CGCG 269-049	7.47 ± 0.05	12	0.794	11, 13
Sextans B (DDO 70)	7.53 ± 0.05	42	30.9	11, 13
UGC 6817 (DDO 99)	7.53 ± 0.05	47	9.33	11, 13
Sextans A (DDO 75)	7.54 ± 0.06	62	12.0	11, 13
UGC 4483	7.56 ± 0.03	33	2.63	11, 13
NGC 4163	7.56 ± 0.14	9.3	40.7	11, 13
UGC 668 (IC 1613)	7.62 ± 0.05	34	13.8	11, 14
UGC 8091 (GR 8)	7.65 ± 0.06	5.9	3.55	11, 13
UGC 7605	7.66 ± 0.11	22	13.2	11, 17
UGC 521	7.67 ± 0.05	290	92.1	11, 18
NGC 3741	7.68 ± 0.05	81	11.2	11, 13
UGC 4278 (IC 2233)	7.69 ± 0.05	160	316	11, 19
UGC 695	7.69 ± 0.12	72	120	11, 20
UGC 5923 (Mrk 1264)	7.79 ± 0.14	42	195	11, 21

^aReferences: 1 - Izotov et al. (2005); 2 - Ekta et al. (2009); 3 - This work; 4 - Skillman et al. (2013); 5 - McQuinn et al. (2013); 6 - Skillman & Kennicutt (1993); 7 - Izotov & Thuan (1999); 8 - van Zee et al. (1998); 9 - Aloisi et al. (2007); 10 - Fisher et al. (2014); 11 - Berg et al. (2012); 12 - Ekta et al. (2008); 13 - Ott et al. (2012); 14 - Hunter et al. (2012); 15 - Izotov et al. (1997); 16 - Pustilnik et al. (2004); 17 - Begum et al. (2008); 18 - Springob et al. (2005); 19 - Stark et al. (2009); 20 - Nicholls et al. (2011); 21 - Haynes et al. (2011)

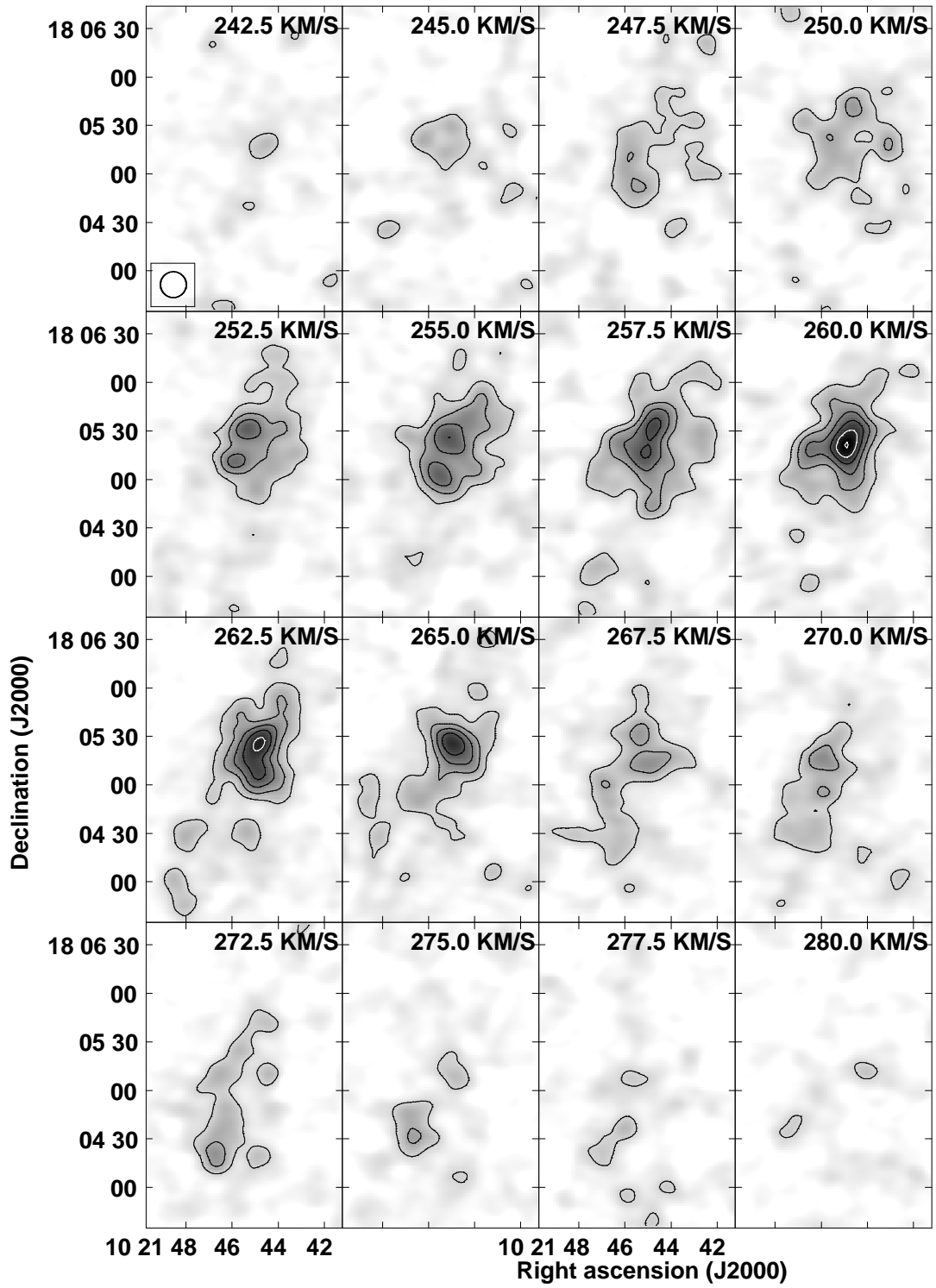


Fig. 1.— Channel maps of HI emission in Leo P at $16''$ resolution (beam shown in upper left panel). The radial velocity is shown in each panel, and the contours show HI at flux levels of (1, 2, 3, 4, 5, 6) mJy Bm^{-1} ; the noise level in the cube is 0.51 mJy Bm^{-1} .

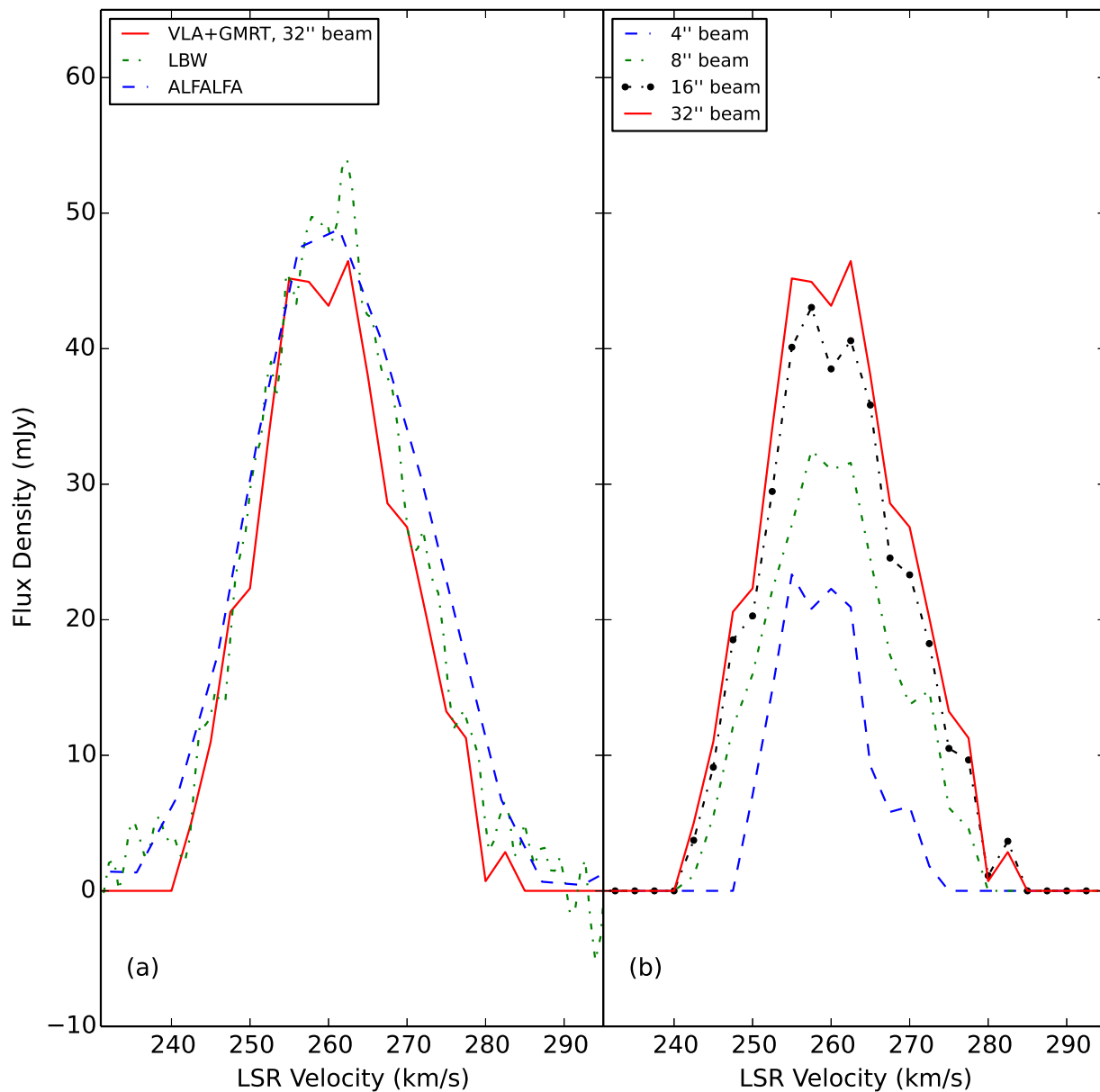


Fig. 2.— (a): Integrated spectra of Leo P from the VLA+GMRT observations at 32'' spatial resolution (solid red line), from the ALFALFA data products (blue dashed line), and from the follow-up Arecibo observation with the LBW receiver at Arecibo (green dashed line). (b) Integrated spectra of Leo P from VLA+GMRT observations at 4'', 8'', 16'', and 32'' spatial resolutions with 2.5 km s^{-1} spectral resolution. As expected, due to masking, the flux density of the source decreases with increasing spatial resolution.

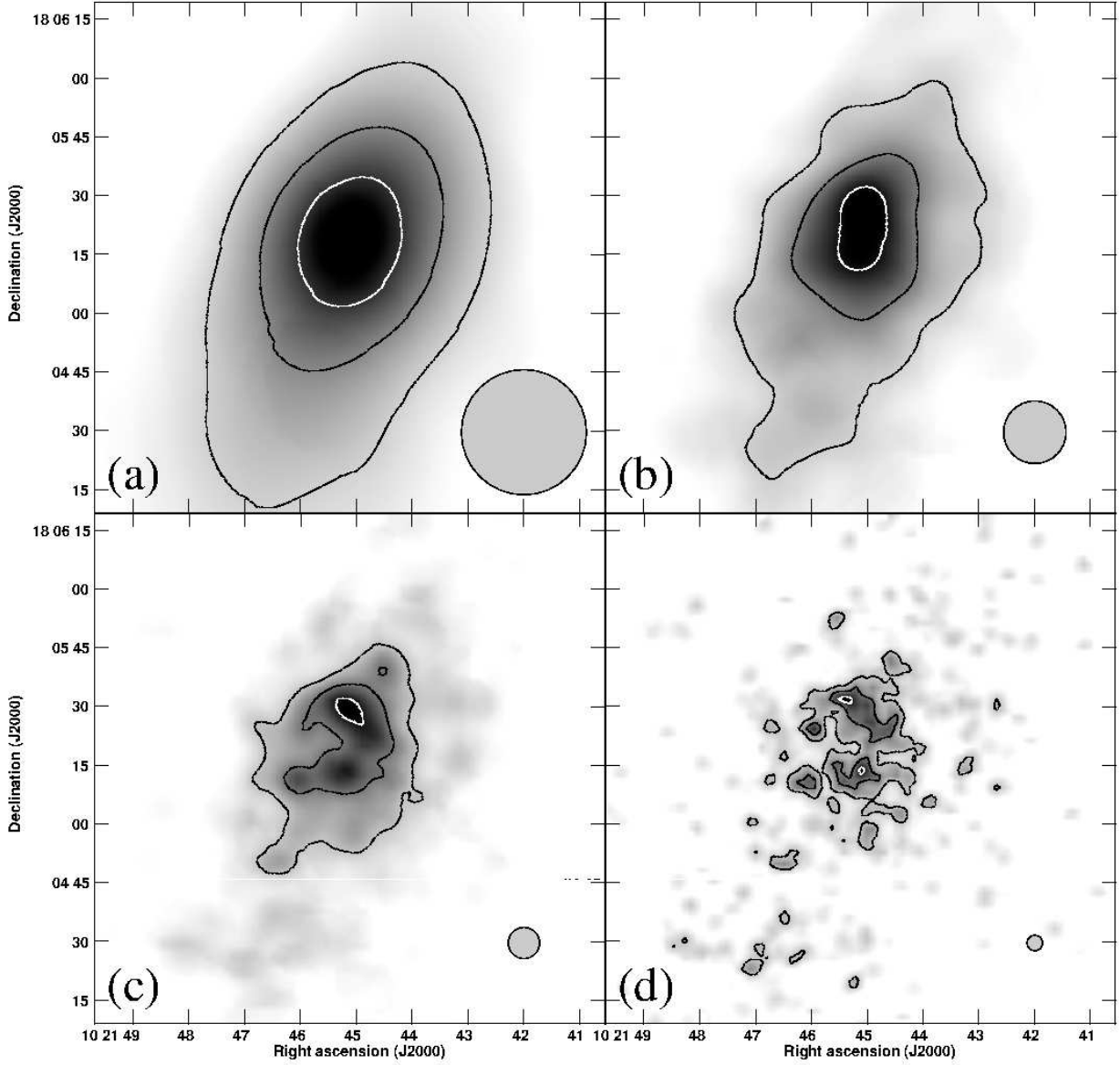


Fig. 3.— H I column density images of Leo P at 32'' (a), 16'' (b), 8'' (c), and 4'' (d) resolutions. The images are shown in greyscale; the column density contours, in units of 10^{20} cm^{-2} , are at levels of (0.75, 1.5, 2.5), (1.0, 2.25, 3.5), (1.5, 3, 4.5), and (2, 4, 6) in panels (a), (b), (c), and (d), respectively. The beam sizes are shown by filled circles in the lower right of each panel. These contours are overlaid on optical images of Leo P in Figure 4.

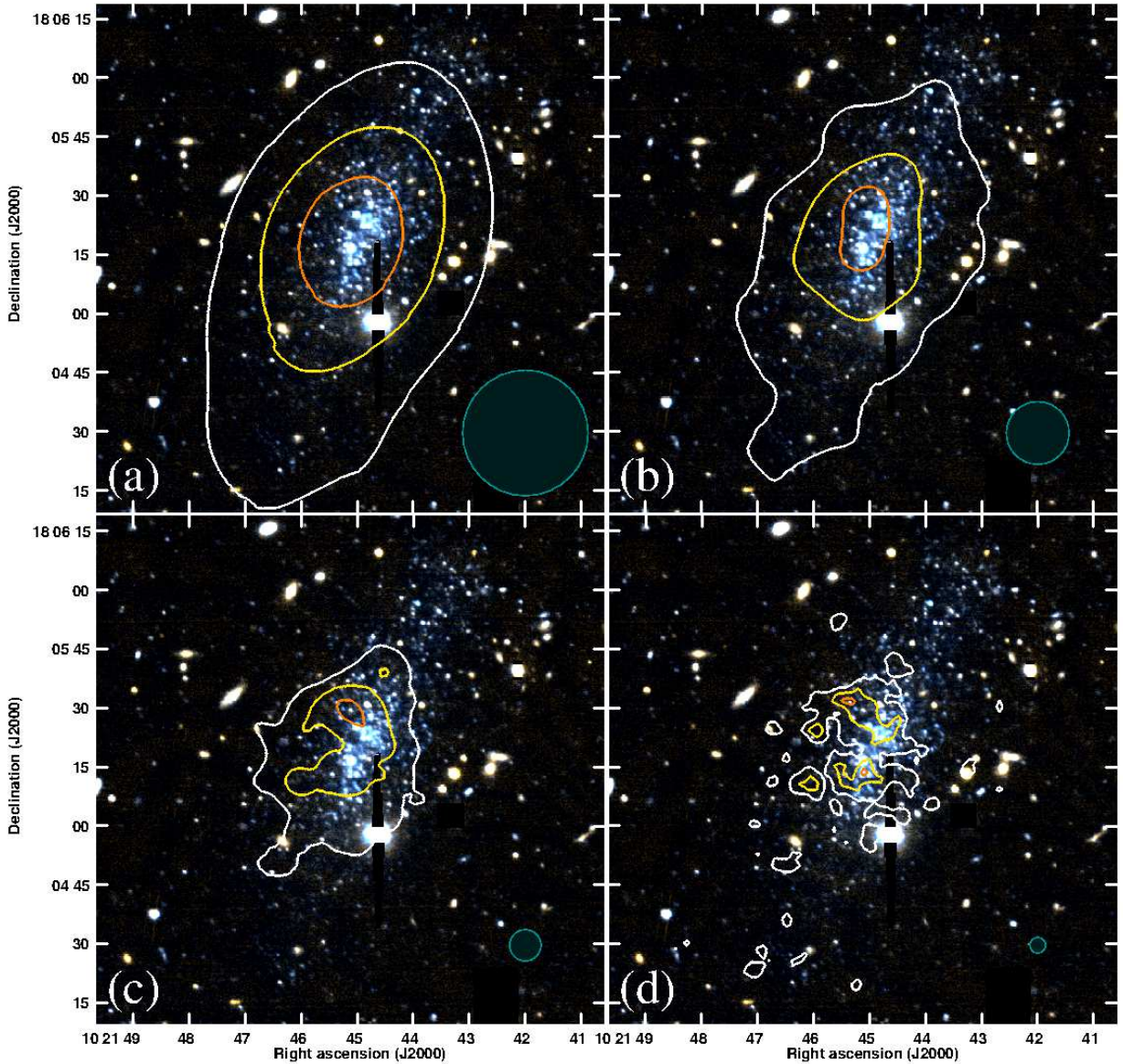


Fig. 4.— HI column density images of Leo P at 32'' (a), 16'' (b), 8'' (c), and 4'' (d) resolutions, overlaid as contours on the optical 3-color image derived from the LBT images presented in McQuinn et al. (2013). HI column density contours are color-coded from lowest (white) to highest (orange) in each panel. The column density contours, in units of 10^{20} cm^{-2} , are at levels of (0.75, 1.5, 2.5), (1.0, 2.25, 3.5), (1.5, 3, 4.5), and (2, 4, 6) in panels (a), (b), (c), and (d), respectively. The beam sizes are shown by filled circles in the lower right of each panel. Note that the HI column density exceeds $6 \times 10^{20} \text{ cm}^{-2}$ in close proximity to the single H II region (see Figure 5 for details). Bleed trails due to bright Milky Way foreground stars have been removed manually.

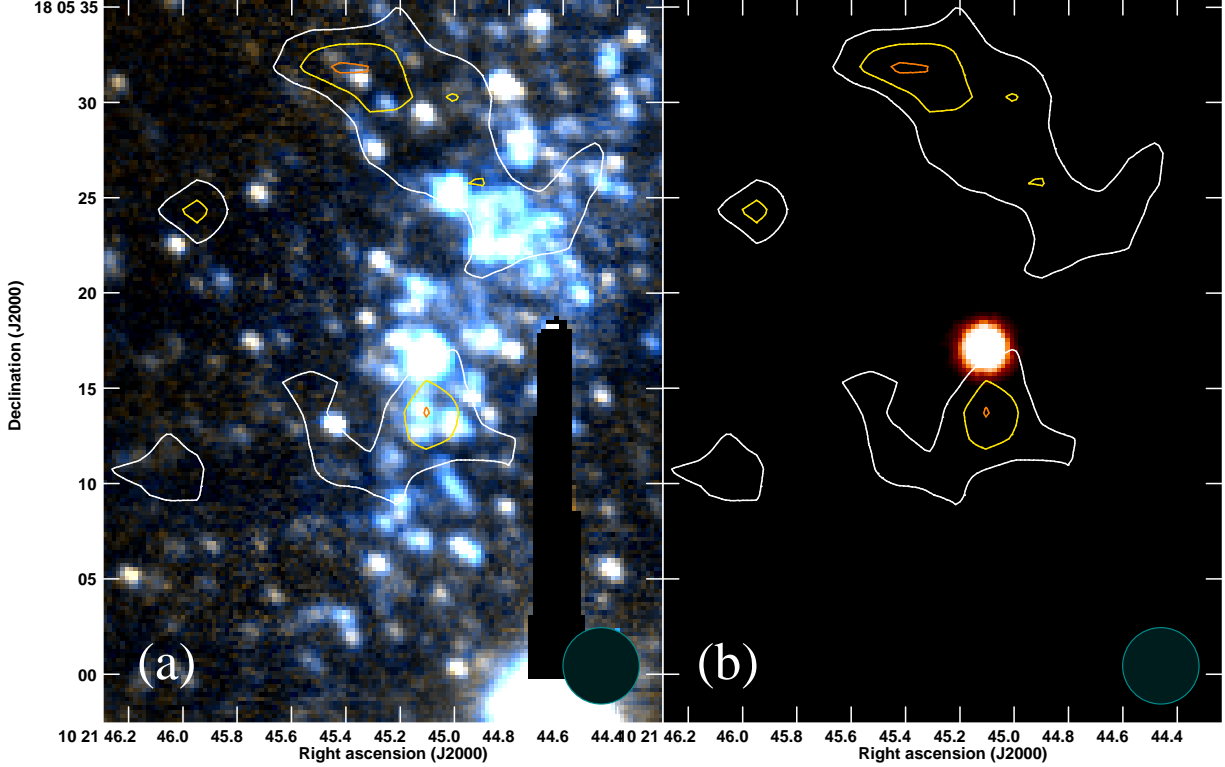


Fig. 5.— HI column density contours at $4''$ resolution, overlaid on LBT 3-color (a) and on WIYN 2.1 m continuum subtracted H α (b) images of Leo P; the field of view is smaller than that shown in Figure 4. Contours are shown at levels of $(4.0, 5.25, 6.5) \times 10^{20} \text{ cm}^{-2}$. The single H II region is in very close proximity to an HI column density maximum ($6.5 \times 10^{20} \text{ cm}^{-2}$). A second column density peak, which is not currently associated with ongoing star formation, is located slightly offset from the main stellar component. The beam size is shown by a filled circle in the lower right of each panel. Bleed trails due to bright Milky Way foreground stars have been removed manually.

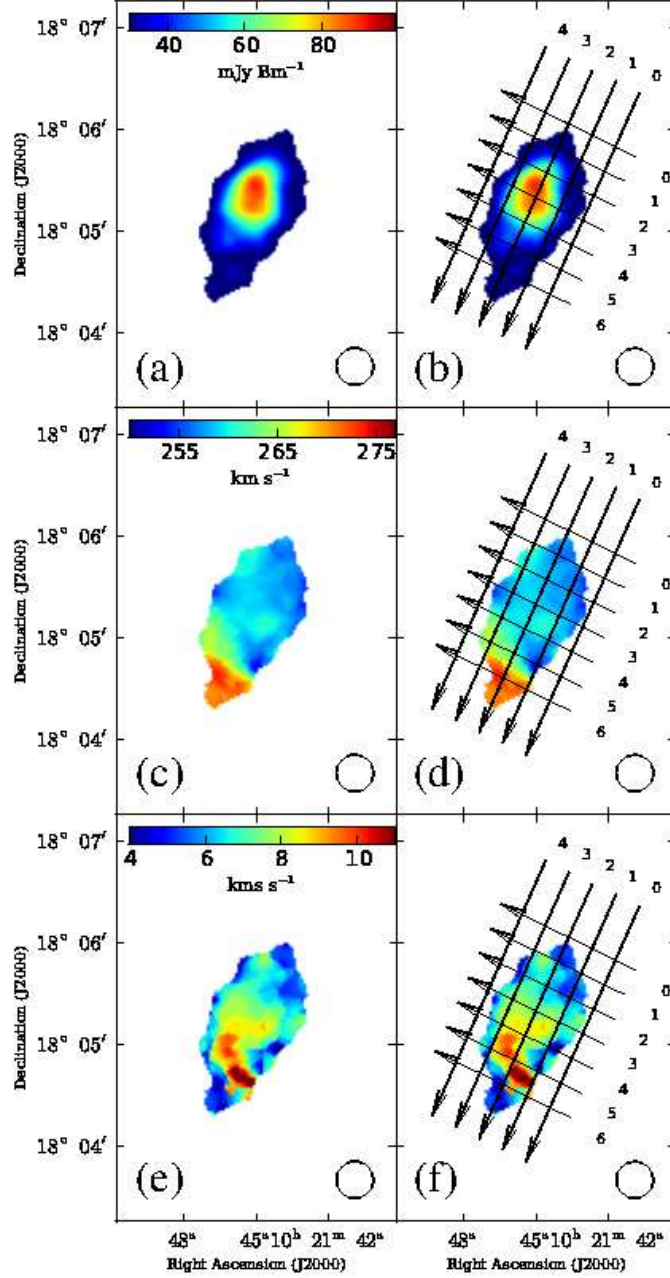


Fig. 6.— (a) + (b): Map of integrated H I emission from the 16'' resolution cube. The beamsize is represented by the circle in the lower-right of each image. (c) + (d): Intensity-weighted H I velocity fields from the same cube. (e) + (f): Intensity-weighted H I velocity dispersion field from the same cube. Panels (b), (d), and (f) are overlaid with arrows representing the direction and length of the position-velocity slices taken. The arrows leading from the northwest to the southeast represent the major-axis position-velocity slices which sample 2.7'. The arrows leading from the southwest to the northeast represent the minor-axis position-velocity slices which sample 1.5'. Major-axis slice 2 and minor-axis slice 3 are centered on the peak column density. Each slice along the major-axis and minor-axis is separated by a beam width; thus each slice is independent of the adjacent slice. The numbers at the origins of the arrows correspond to the frames in Figure 7.

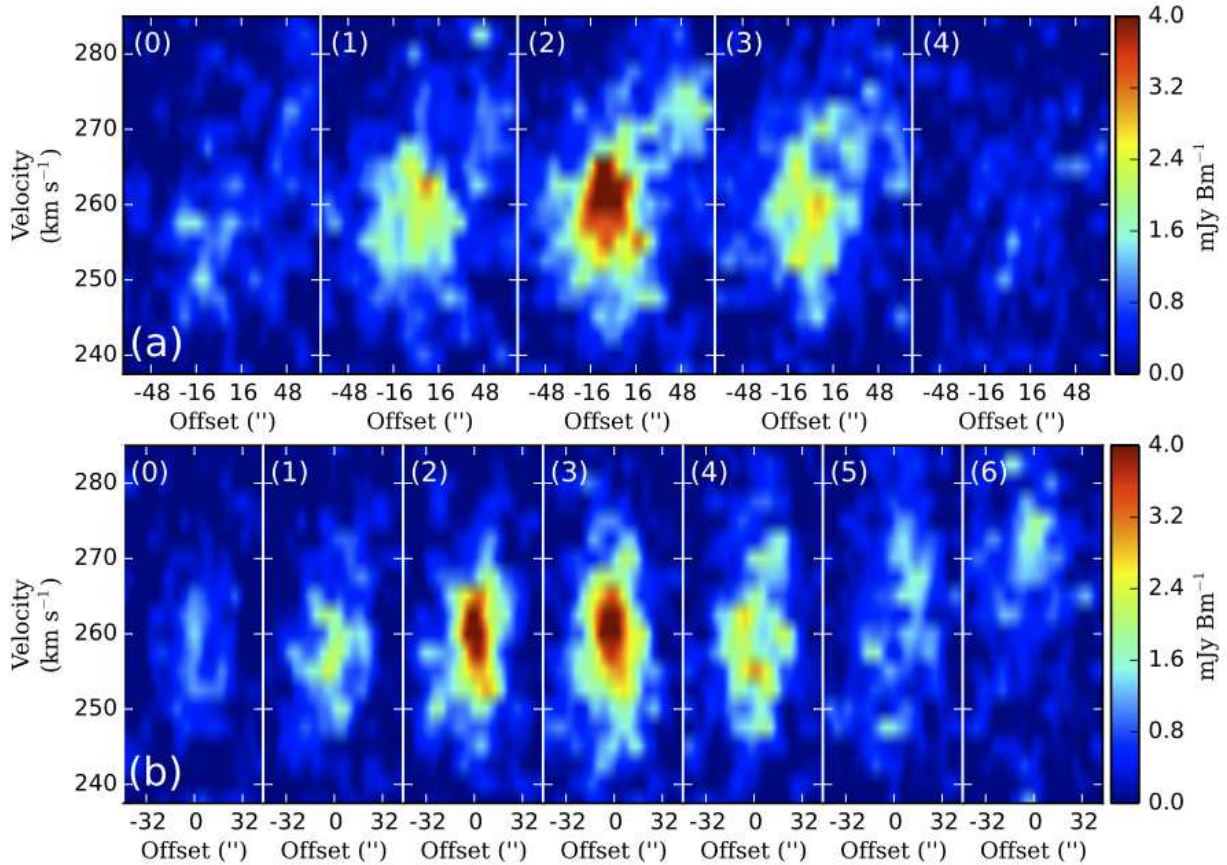


Fig. 7.— (a) Major-axis position-velocity slices of the neutral gas in Leo P separated by a beam width at 16'' resolution. (b) Same as (a) except for the minor-axis. Each slice averages pixels over a beamsize, and is completely independent from an adjacent slice. See Figure 6 for an illustration of the slices taken. The apparent slope in the velocity distribution between the minor-axis slices can be interpreted as rotation. The velocity dispersion as shown by the extended emission across many velocities is only slightly lower than any apparent rotational velocity seen in Leo P.

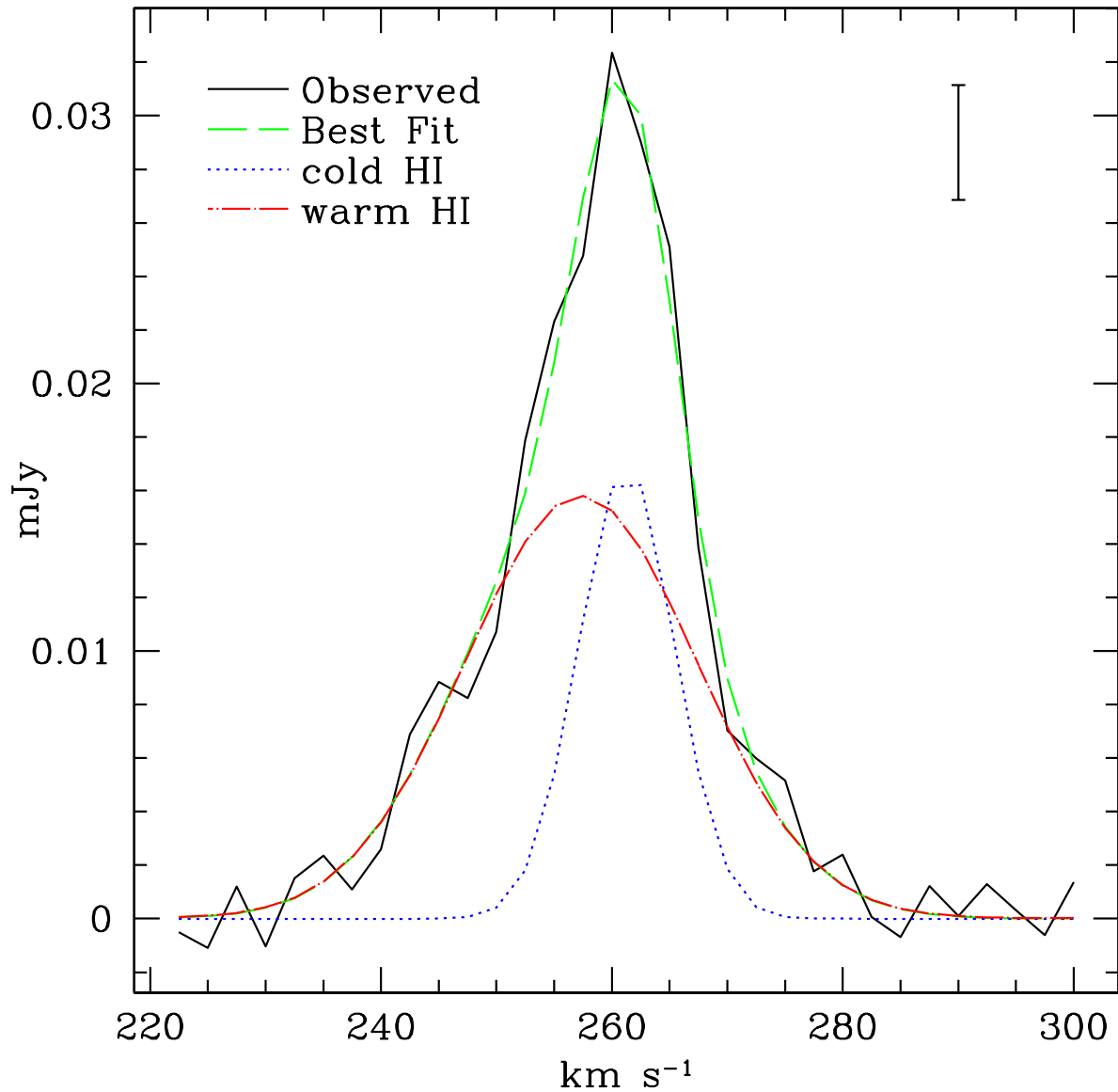


Fig. 8.— The spectrum at the location of the peak cold HI component detected in Leo P at 24'' (200 pc) resolution. The cold HI component represents 30% of the total HI flux in the peak location. The error bar in the upper right represents the error of the spectrum derived from the non-flux-rescaled cube of $0.64 \text{ mJy beam}^{-1}$ (0.002 mJy). The warm HI component has a velocity width of $10.08 \pm 1.15 \text{ km s}^{-1}$ and the cold HI component has a velocity width of $4.18 \pm 0.86 \text{ km s}^{-1}$. Assuming a thermalized distribution of particles without turbulence, these widths correspond to kinetic temperatures of 6160 K and 1060 K for the warm and the cold components, respectively.

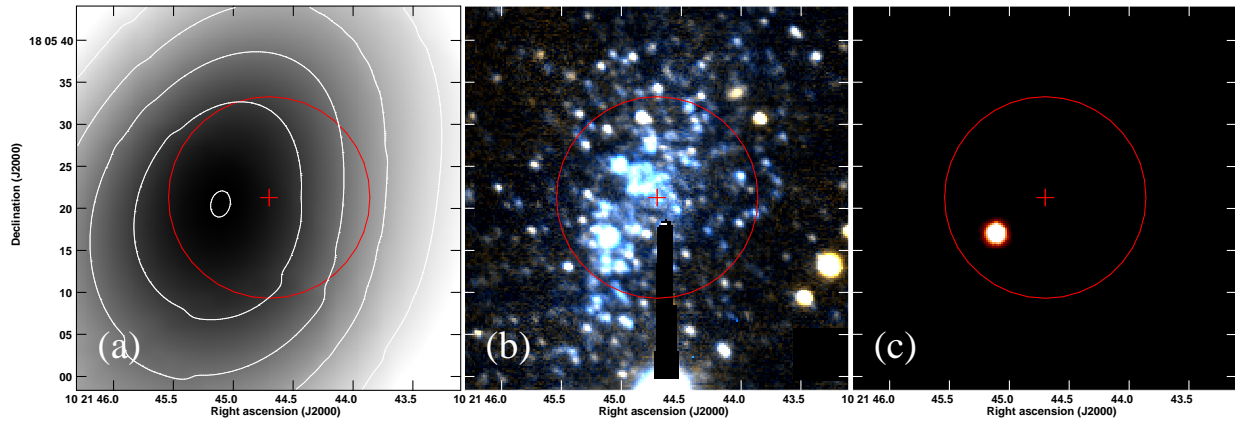


Fig. 9.— HI image at $24''$ resolution (a), LBT color image (b), and H α image (c), each overlaid with a 200 pc diameter red circle representing the location of the (unresolved) cold HI component. The contours on the HI image range from $(0.8\text{--}3.8) \times 10^{20} \text{ cm}^{-2}$ in steps of $5 \times 10^{19} \text{ cm}^{-2}$. The exact location of the cold HI within the $24''$ beam is uncertain due to the unresolved nature of the emission.

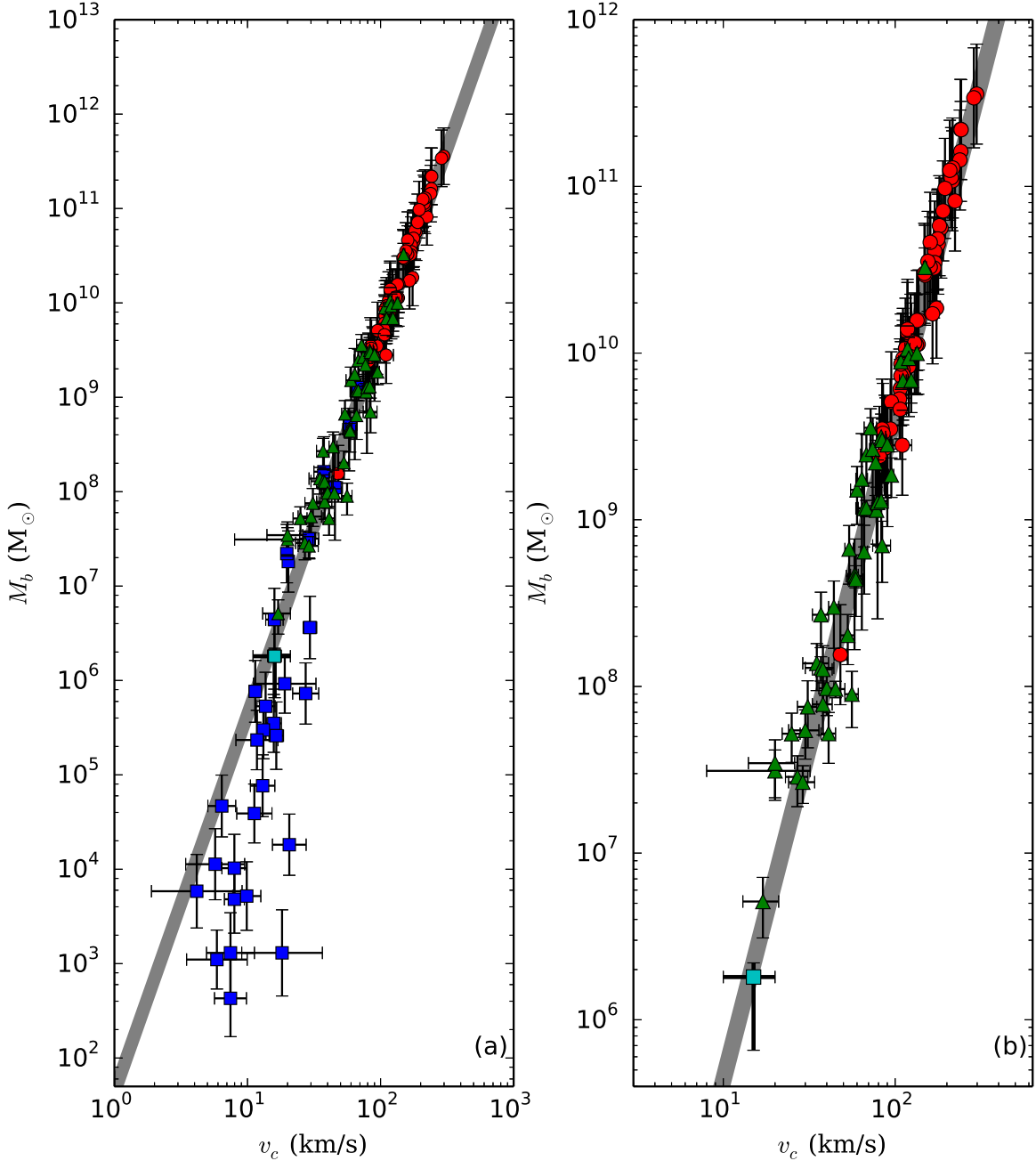


Fig. 10.— Reproductions of the baryonic Tully-Fisher relation (BTFR) from McGaugh (2012). Baryonic masses are plotted against the circular velocities of galaxies; red circles are star-dominated galaxies, green triangles are gas-rich galaxies, and blue squares are dSph galaxies. The shaded grey line shows the $\pm 1\sigma$ regression to the properties of the gas-dominated derived in McGaugh (2012). The turquoise square represents Leo P. Panel (a) shows all galaxies from McGaugh (2012), while panel (b) removes the dSph systems and compresses the dynamic range for ease of interpretation. The data point for Leo P is plotted at the rotational velocity of 15 km s^{-1} derived in § 4. Leo P is the slowest rotating gas-rich galaxy studied to date. The position of Leo P in these plots is consistent with the preliminary estimate presented in Giovanelli et al. (2013).

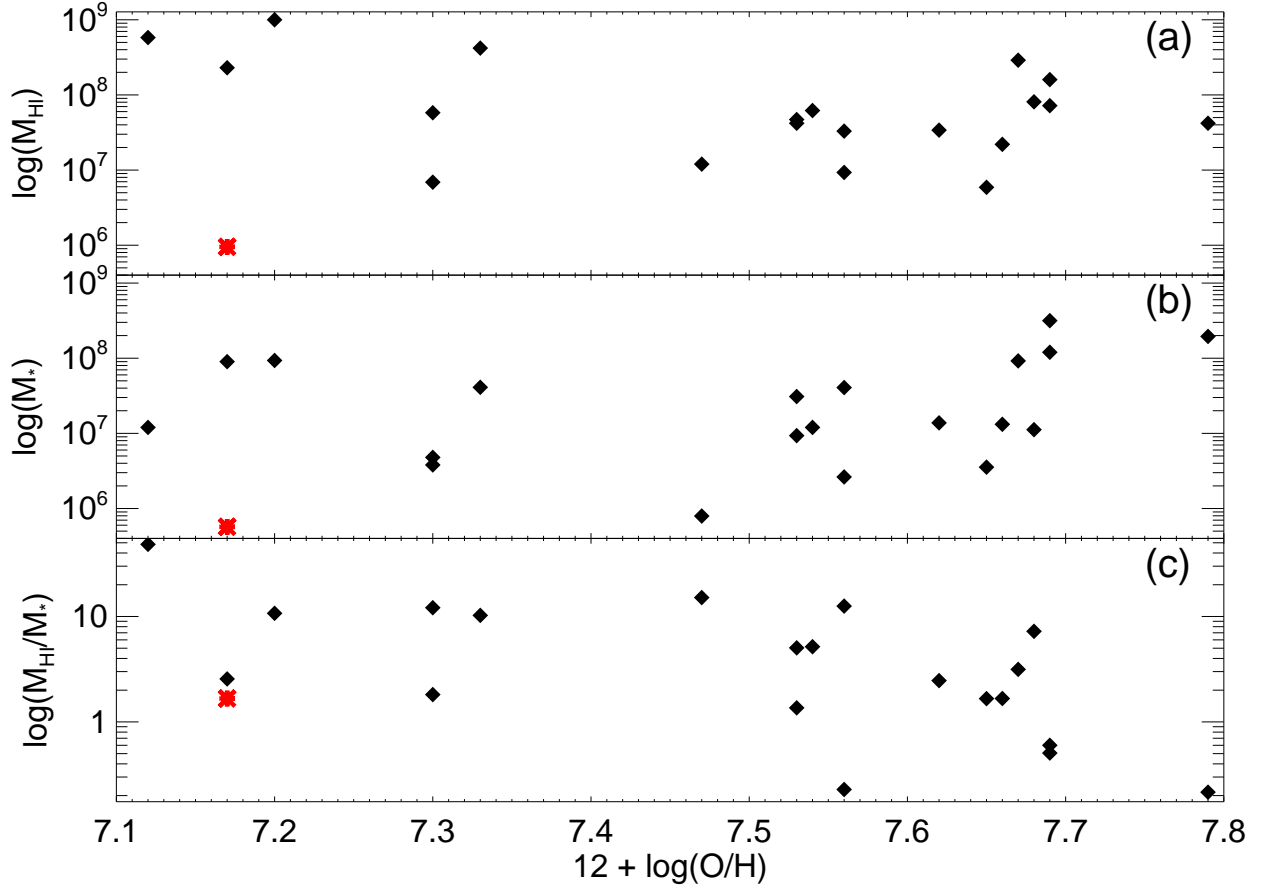


Fig. 11.— The HI mass (a), stellar mass (b), and the ratio of HI mass to stellar mass (c), plotted versus oxygen abundance for selected XMD galaxies. Leo P is shown in red in each panel. The parameters of each galaxy are found in Table 2.